

1 **Back-arc extension in the Andaman Sea: tectonic and**
2 **magmatic processes imaged by high-precision**
3 **teleseismic double-difference earthquake relocation**

4

5 **Diehl, T., Waldhauser, F., Cochran, J.R., Kamesh Raju, K.A., Seeber, L., Schaff, D.**
6 **and Engdahl, E.R.**

7

8 **T. Diehl (Corresponding Author):**

9 Lamont-Doherty Earth Observatory, Columbia University, Palisades, New York 10964,
10 USA

11 Now at: Swiss Seismological Service, ETH Zurich, Sonneggstrasse 5, CH-8092, Zurich,
12 Switzerland, Email: tobias.diehl@sed.ethz.ch, Phone: +41 44-632-0498

13

14 **F. Waldhauser, J.R. Cochran, L. Seeber, D. Schaff:**

15 Lamont-Doherty Earth Observatory, Columbia University, Palisades, New York 10964,
16 USA

17

18 **K.A. Kamesh Raju:**

19 National Institute of Oceanography, Dona Paula, Goa 403 004, India

20

21 **E.R. Engdahl:**

22 Department of Physics, University of Colorado, Boulder, Colorado 80309, USA

23 **Abstract**

24 The geometry, kinematics, and mode of back-arc extension along the Andaman Sea plate
25 boundary are refined using a new set of significantly improved hypocenters, global CMT
26 solutions, and high-resolution bathymetry. By applying cross-correlation and double-
27 difference algorithms to regional and teleseismic waveforms and arrival times from ISC
28 and NEIC bulletins (1964-2009), we resolve the fine-scale structure and spatio-temporal
29 behavior of active faults in the Andaman Sea. The new data reveal that back-arc
30 extension is primarily accommodated at the Andaman Back-Arc Spreading Center
31 (ABSC) at $\sim 10^\circ$, which hosted 3 major earthquake swarms in 1984, 2006, and 2009.
32 Short-term spreading rates estimated from extensional moment tensors account for less
33 than 10% of the long-term 3.0-3.8 cm/yr spreading rate, indicating that spreading by
34 intrusion and the formation of new crust make up for the difference. A spatio-temporal
35 analysis of the swarms and Coulomb-stress modeling show that dike intrusions are the
36 primary driver for brittle failure in the ABSC. While spreading direction is close to ridge-
37 normal, it is oblique to the adjacent transforms. The resulting component of E-W
38 extension across the transforms is expressed by deep basins on either side of the rift and a
39 change to extensional faulting along the West Andaman Fault system after the $M_w=9.2$
40 Sumatra-Andaman earthquake of 2004. A possible skew in slip vectors of earthquakes in
41 the eastern part of the ABSC indicates an en-echelon arrangement of extensional
42 structures, suggesting that the present segment geometry is not in equilibrium with
43 current plate-motion demands and thus the ridge experiences ongoing re-adjustment.

44

44 **1. Introduction**

45 The Andaman Sea in the northeast Indian Ocean is an actively opening marginal basin
46 inboard of the Western Sunda Arc (Figure 1). Extension in the Andaman Sea is primarily
47 driven by oblique subduction of the Indian-Australian plate beneath the western Sunda
48 arc, in contrast to back-arc basins in the southwestern Pacific, where extension is mainly
49 associated with trench-rollback [e.g., *Uyeda and Kanamori, 1979*]. Oblique plate
50 convergence is accommodated in part by strain partitioning along this subduction zone
51 resulting in arc-parallel strike-slip faulting and the formation of a northward-moving
52 sliver plate [e.g., *Fitch, 1972; McCaffrey, 1992; McCaffrey, 2009*]. The boundary
53 between the sliver, Burma Plate, and the Sunda Plate is a system of arc-parallel
54 transforms and arc-normal ridges in the back-arc of the Andaman Sea, which connects to
55 the right-lateral Sumatra Fault along the volcanic arc in the southwest (Figure 1). The
56 connection with the Sagaing Fault to the northeast is less distinct and different geometries
57 have been proposed [e.g., *Rangin et al., 1999; Curray, 2005*; see Figure 1]. As the
58 Burma-Plate is dragged northwards (with respect to the Sunda-Plate) by the
59 underthrusting Indian-Australian plate, ‘pull-apart’ basins develop along the plate
60 boundary, resulting in NE-SW extension of the Andaman Sea [e.g., *Curray, 2005*;
61 *McCaffrey, 2009*]. While the term ‘pull-apart’ usually refers to intracrustal extension
62 along a strike slip system, extension in the Andaman Sea involves the formation of new
63 crust [*Kamesh Raju et al., 2004*] and justifies identifying the sliver as a distinct plate.
64 This transtensional mode of back-arc opening is also referred to as ‘rhombochasm’ [e.g.,
65 *Rodolfo, 1969; Curray, 2005*] or ‘leaky-transform’ [e.g., *Thompson and Melson, 1972*;
66 *Uyeda and Kanamori, 1979; Taylor et al., 1994*].

67

68 The first geophysical evidence for active opening of the Andaman Sea was derived from
69 bathymetric, magnetic, gravimetric, heat flow, and seismic surveys [e.g., *Rodolfo*, 1969;
70 *Curray et al.*, 1979; for a summary see *Curray*, 2005]. *Kamesh Raju et al.* [2004] mapped
71 the structure of the Andaman Back-Arc Spreading Center (ABSC, Figure 1) in detail,
72 using high-resolution multibeam swath bathymetry in combination with magnetic and
73 single channel seismic surveys. They identify three SW-NE trending spreading segments,
74 separated by left-stepping offsets of several kilometers. Interpretation of magnetic
75 anomalies suggests that true seafloor spreading started at about 4 Ma and is thus much
76 younger than the Sunda arc. It may still be developing, according to the kinematic model
77 of *Kamesh Raju et al.* [2004] that implies a westward propagation of the spreading center.
78 Magnetic anomalies suggest an initial spreading rate of 1.6 cm/yr and an increase in rate
79 up to 3.8 cm/yr from about 2-2.5 Ma to present [*Kamesh Raju et al.*, 2004]. The
80 estimated 118 km opening of the ABSC over 4 Myr results in an average rate of 3.0
81 cm/yr [*Curray*, 2005]. *Chamot-Rooke et al.* [2001] proposed a similar range of spreading
82 rate of 2.8-3.6 cm/yr. With a present full rate in the range of 3.0-3.8 cm/yr, the Andaman
83 Spreading Center is in the class of slow-spreading ridges [e.g., *Dick et al.*, 2003].

84

85 Early evidence for neotectonic extension was based on focal mechanisms determined
86 from teleseismic records of earthquakes in the Andaman Sea. *Fitch* [1972] found three
87 normal faulting events in the northern part of the Andaman Sea, indicating a WNW-NW
88 extension. In addition, he associated four right-lateral strike slip events located north and
89 northwest of Sumatra with a submarine continuation of the Sumatra fault system. The

90 existence of two spreading centers located at 10°N and at 14°N separated by a N-S
91 transform fault was inferred from the recovery of additional right-lateral strike slip and
92 normal faulting mechanisms in the Andaman Sea by *Eguchi et al.* [1979]. *Guzman-*
93 *Speziale and Ni* [1993] obtained the strikingly low short-term spreading velocity of 0.05
94 cm/yr in the Andaman Sea from summing seismic moment tensors of normal faulting
95 events between 1964 and 1986, much smaller than the calculated displacement velocity
96 along the right-lateral Sagaing Fault. Their spreading velocity was based on the
97 assumption of full coupling in a deeply rooted extension regime with no contribution
98 from magmatic injection and is likely an underestimate.

99

100 Earthquakes in the Andaman Sea often occur clustered in space and time as noted e.g. in
101 *Mukhopadhyay and Dasgupta* [2008] and shown in Figure S1. In the course of this study
102 we use the term ‘cluster’ to indicate spatial clustering and ‘sequence’ for spatial as well
103 as temporal clustering of earthquakes. Special types of sequences are ‘swarms’, which
104 typically lack a distinct mainshock, show an unusually large spatial extent compared to
105 the moment release of the largest individual event, and magnitudes fail to decay with
106 time [e.g., *Roland and McGuire*, 2009]. The characteristics of several earthquake
107 sequences in the Andaman Sea are described in detail in section S.1 of the electronic
108 supplement. Earthquake swarms are observed in 1973, 1983-1984 and 1993, particularly
109 in the south Andaman Sea (Figure 2 and S1-S2). In March 2006, more than one year after
110 the Mw=9.2 December 2004 Sumatra-Andaman earthquake, an earthquake swarm
111 occurred in the ABSC, followed by another swarm in July 2009 (Figure 2 and S1-S2).
112 The swarm-like occurrence of earthquakes is indicative of episodic rifting events. Major

113 earthquake swarms in the ABSC appear to occur roughly every ten years, with the
114 exception of the 2009 swarm, which occurred after a quiescence of only three years
115 (Figure S1).

116

117 Existing models of plate-boundary structure and tectonic processes in the Andaman Sea
118 are based in large part on global bulletin locations and associated focal mechanisms.
119 Bulletin locations such as provided by the ISC (International Seismological Centre) or
120 EDR (Earthquake Data Report of the National Earthquake Information Center, NEIC)
121 typically have spatial resolution (depth in particular) below the scale-length of tectonic
122 structures in this region and hamper seismotectonic interpretations. To better understand
123 the underlying mechanisms of the earthquake swarms in the Andaman Sea, we use cross-
124 correlation and double-difference methods to significantly improve the hypocenter
125 locations in standard global earthquake catalogs. The high-resolution time-space
126 seismicity patterns together with global CMT-solutions starting in 1976
127 (<http://www.globalcmt.org>) and detailed seafloor bathymetry are combined to construct
128 and discuss an improved seismotectonic framework for the Andaman Back-Arc region.

129

130 **2. Data and Double-Difference Relocation**

131 We use phase arrival time data observed at regional and global seismic networks and
132 published in the ISC bulletin for the years 1964-2006 and in the EDR bulletin for the
133 years 2007-2009, as well as digital waveform data obtained from the Incorporated
134 Research Institutions for Seismology (IRIS). The combined ISC/EDR catalog includes a
135 total of 19,000 earthquakes in the Sumatra-Andaman region, 1,266 of which occurred in

136 the Andaman Sea (area outlined by dashed line in Figure 2) and are discussed in this
137 paper. The hypocenters in these catalogs are estimated using single event location
138 methods that invert arrival times for the absolute location of the hypocenter and its origin
139 time. Due to limited station coverage, inconsistencies in phase association, uncertainties
140 in arrival time readings, and errors in the model used to predict the data, the spatial
141 resolution of these locations is often low. Because of the trade-off between origin time
142 and depth for events recorded at teleseismic distances, focal depths are often
143 unconstrained and set to a default value.

144

145 Previous relocation studies include *Engdahl et al.* [2007], who relocated a subset of the
146 global bulletin data for the Sumatra-Andaman region following the EHB procedure,
147 which computes a groomed catalog of the highest-quality events with improved depths by
148 using depth phases obtained by probabilistic phase association [*Engdahl et al.*, 1998].
149 *Pesicek et al.* [2010] relocated the EHB catalog by applying a double-difference
150 algorithm to first arriving P waves and depth phases extracted from the EHB bulletin and
151 measured via waveform cross-correlation together with a regional 3D velocity model.

152

153 In this study we aim to resolve and study in a comprehensive way the fine details of
154 active faulting in the Andaman Sea by applying the teleseismic double-difference
155 (hypoDD) algorithm of *Waldhauser and Schaff* [2007] to all first and later arriving P and
156 S phase data reported in the ISC and EDR bulletins. The double-difference method
157 removes unmodeled velocity structure by directly inverting travel-time differences
158 between events for their hypocenter separation [*Waldhauser and Ellsworth*, 2000]. This

159 approach permits the combined use of phase delay times measured from bulletin picks
160 and from cross-correlation of similar seismograms. Cross-correlation (CC) methods can
161 measure differential phase arrival times with subsample precision for events that are
162 nearby and have similar focal mechanisms, typically resulting in more than an order of
163 magnitude improvement over delay times formed from phase onset picks reported in
164 earthquake bulletins [*Poupinet et al.*, 1984; *Waldhauser and Schaff et al.*, 2007].

165

166 **2.1 Waveform cross-correlation**

167 While the following cross-correlation results pertain to the entire Sumatra-Andaman
168 region, their subsequent analysis and interpretation focuses on the Andaman Sea. We
169 extracted 7 million waveforms of more than 19,000 events from the IRIS and GEOFON
170 data centers, selecting the best ~1000 regional and global stations from the Global
171 Seismic Network (GSN), the GEOFON network, and the GEOSCOPE network. All
172 available stations within a radius of 30° from the Sumatra-Andaman region, and all
173 available stations in the southern hemisphere were used. Typically less than 10 records
174 are available for events that occurred prior to 1990, and none for events before 1984. We
175 perform time-domain cross-correlation [*Schaff et al.*, 2004; *Waldhauser and Schaff,*
176 *2007*] on 9 s long windows around the predicted first arriving P and S phases. Waveforms
177 of all pairs of events separated by less than 300 km are cross-correlated. A band-pass
178 filter of 0.5 to 2.0 Hz is applied to seismograms prior to cross-correlation in order to
179 increase the signal-to-noise ratio of the body waves.

180

181 The distribution of the CC measurements across the Sumatra-Andaman region is shown
182 in Figure 3. Colors indicate percentage of correlating events within bins of 50 x 50 x 50
183 km. We exclude deeper events in Figure 3 to show the correlation results for crustal
184 events in the back-arc discussed later. We define a correlated event as event that has at
185 least four CC-measurements with correlation coefficients ≥ 0.8 with at least one
186 neighboring event. High numbers of correlating events occur up-dip of the nucleation of
187 the 2004 Sumatra-Andaman and 2005 Nias megathrust earthquakes, beneath the Aceh-
188 Basin (AB, Figure 3), in the region of the January 2005 Nicobar-Swarm [e.g., *Kundu et*
189 *al.*, 2012], along the Andaman Spreading Center, and at the NE edge of the Alcock Rise
190 (AR, Figure 3). We associate these patches of high correlation as regions of increased
191 earthquake density where earthquakes appear to rupture the same faults with similar slip
192 orientations. Beneath the Aceh-Basin, for example, such repeated slip occurs on the
193 megathrust and on imbricate faults in the mantle wedge [*Waldhauser et al.*, 2012]. Low
194 numbers of correlating events occur along the volcanic arc and the Sumatra Fault System
195 (Figure 3), which is likely due to the complex and highly segmented fault structures on-
196 shore northern Sumatra [*Sieh and Natawidjaja*, 2000].

197

198 **2.2 Teleseismic multiphase double-difference relocation**

199 We combine 40,000 high-precision correlation delay-time measurements for events
200 within the back-arc region with 1.3 million delay times formed from bulletin picks and
201 invert the data for relative hypocenter locations using the teleseismic hypoDD algorithm
202 of *Waldhauser and Schaff* [2007]. In order to reduce the number of outliers caused by
203 cycle skipping in the correlation data, only CC measurements with CC coefficient ≥ 0.8

204 are used. We compute pick delay times from all first and later arriving P and S phase data
205 listed in the ISC/EDR bulletins. The use of core phases with their steep take-off angles, in
206 addition to depth phases, is especially important to constrain relative depths. The global
207 travel time model ak135 is used to predict the observed data. To reduce the impact of the
208 inhomogeneous station distribution, we selected for each event pair independently the
209 best station within bins of 3 degree across the globe before relocation (see *Waldhauser*
210 *and Schaff* [2007] for details).

211

212 To reduce the often significant errors in the ISC and EDR bulletin locations, which can
213 lead to an incomplete network of delay time links, we relocate each event listed in these
214 catalogs individually relative to events in an updated (1918-2009) and DD relocated
215 version of the EHB catalog for the Sumatra-Andaman region [*Engdahl et al.*, 2007] using
216 a single-event DD algorithm [*Waldhauser*, 2009; *Waldhauser et al.*, 2012]. The improved
217 single-event DD locations are subsequently used to generate a new network of phase
218 delay times from the combined ISC and EDR bulletins, and are taken as starting locations
219 for a final simultaneous inversion of both correlation and phase pick delay time data. The
220 final DD relocations have an RMS of 0.72 s for bulletin pick data. The RMS value for
221 correlation data is on the order of 60 ms for earthquakes with well correlated
222 seismograms, such as observed in cluster C1 (Figure 3 and 4b).

223

224 Figure 4 demonstrates the improvement of the DD-locations compared to the ISC/EDR
225 bulletin locations for two clusters of earthquakes near 12.4°N/95°E (C1 in Figure 3) and
226 12.8°N/95.5°E (C3 in Figure 3). While the ISC/EDR epicenters widely scatter (Figure

227 4a), the DD-locations resolve a NE-SW striking structure (Figure 4b), consistent with the
228 fault-strike of the CMT solutions and the NE-SW oriented structures present in the
229 bathymetry data near the Alcock Rise (Figure 1). DD-locations of cluster C3 (Figure 4d)
230 show that the three sequences occupy distinct areas of the basin suggesting differences in
231 their underlying tectonic mechanisms. Relative location errors, computed from 200
232 bootstrap samples drawn from the final residual vector for each event (see *Waldhauser*
233 *and Ellsworth* [2000] for details), are on the order of few kilometers or less. They are
234 shown in Figure 4 as horizontal projections of the 90% confidence ellipsoids. Relocations
235 of events prior to the 1990's and back to 1964 are mainly or entirely based on bulletin
236 pick data and therefore the quality of the DD-locations may also vary with time.

237

238 **2.3 Assessment of absolute location robustness**

239 Because the EHB locations are the reference base for the overall absolute location of the
240 DD solutions, possible bias in the EHB locations would also affect the absolute position
241 of the DD-solutions. Such bias may result from deviations of the true structure from the
242 1D velocity model ak135 used to locate the events (presence of slab, etc.) and bias in
243 station geometry. Grid search results using the 3D regional velocity model of
244 *Widiyantoro and van der Hilst* [1997] indicate that our absolute locations are robust
245 within 5 km. While relative depths are typically well constrained by differential depth
246 and core phases, the absolute depths in our DD catalog are mostly constrained by depth
247 phases from the EHB bulletin. More details on absolute location robustness are provided
248 in section S.2 of the electronic supplement.

249

250 **3. Seismic structure and kinematics of the Andaman Sea plate boundary**

251 The relocated seismicity and CMT solutions (Figure 5 and 6) image a system of active
252 normal and strike-slip faults that connect the right-lateral Sumatra, Seulimeum and West
253 Andaman transform faults in the southwest with the Sagain Fault in the northeast,
254 forming the present eastern edge of the Burma Plate [*Curray, 2005; Cochran, 2010*]
255 (Figure 1). The majority of earthquakes occur along the extensional plate boundary in the
256 ABSC (Table 1), with intraplate earthquakes (such as I1-I4 in Figure 6) accounting for
257 less than 2% of the total seismic moment in the back-arc region. CMT solutions along the
258 fault system connecting the ABSC with the Sagain Fault (NE-BARC region in Figure 6)
259 are sparser but bigger (i.e. lower b-value) relative to the ABSC (Figure S6 and S7, see
260 section S.3 of the electronic supplement for more details on the b-value analysis) and
261 earthquakes cluster in both space and time as demonstrated by cluster C1 and C2 (Figure
262 6, Table 1). Earthquakes in cluster C1 and C2 locate east of the NS trending transform
263 faults and seafloor depression and show primarily extensional failure along ~20 km long
264 NE-SW striking faults. These faults abut the NS striking transform fault and presumed
265 plate boundary (Figure 4b and 6).

266

267 Cluster C1 is formed by a sequence of extensional events ($M_w=4.8-5.8$) (N1-8, Figure
268 4b) that started in July 2007 and lasted for less than a year. The distribution of
269 magnitudes with time in Figure S3 suggests a foreshock-mainshock-aftershock pattern
270 and the b-value of cluster C1 is close to 1 (Figure S7). The sequence was preceded, by
271 one year, by two right-lateral, strike-slip earthquakes ($M_w=5.1$ and 5.3) that ruptured the
272 adjacent transform fault within one hour of each other (S1-2, Figure 4b). The structure

273 and kinematics of the seismicity that forms cluster C2 are comparable to C1, suggesting a
274 similar process ~60 km south of C1.

275

276 Another distinct earthquake cluster is revealed in the northeastern part of the basin (C3,
277 Figure 4d and 6). The position and orientation of this 35 km long cluster correlate with a
278 NE-SW striking seafloor depression, which is interpreted as a short spreading axis by
279 *Curray* [2005]. The majority of earthquakes associated with C3 occurred within three
280 sequences (12/1983, orange; 01/1984, yellow; 01/2003, blue; Figure 4d) that occupy
281 distinct areas. The 1983 sequence initiated in the center of the bathymetric depression and
282 activated faults along the northern rim of the basin and beyond to the northeast. The 1984
283 and 2003 sequences flanked the 1984 sequence at its SW and NE termination. The
284 sequences in 1983 and 1984 have the character of earthquake swarms, whereas the first
285 sequence in January 2003 indicates a mainshock-aftershock pattern (Figure S4).

286

287 **3.1 Spatio-temporal characteristics of ABSC seismicity**

288 Three major swarms that occurred in 1984, 2006, and 2009, and two smaller ones in 1973
289 and 1993, dominate the seismicity along the ABSC (Figure 2 and S1-S2, Table 2). CMT
290 solutions are almost exclusively pure normal faulting mechanisms with some variation in
291 strike and dip (Figure 5 and 6). The analysis of non-double-couple components of global
292 CMT solutions, described in detail in section S.4 of the electronic supplement, identified
293 a possible vertical compensated-linear-vector-dipole (CLVD) mechanism within the 1984
294 swarm (vPC1 in Figure 5). Figure 7a shows the high-resolution bathymetry data for the
295 seismically active central part of the spreading ridge with DD locations superimposed

296 (dots color coded according to swarm occurrence). Based on the bathymetry data and
297 magnetic anomalies the ABSC is divided into three segments A, B, and C (brown lines in
298 Figure 7a) [*Kamesh Raju et al.*, 2004].

299

300 The smallest swarm occurred in July 1973 (magenta dots in Figure 7a) at the western end
301 of segment A. It contains 6 events and its duration was less than a day.

302

303 The swarm of July 1984 includes ~80 events (blue dots in Figure 7a) and occupied
304 approximately 40 km of the central part of the eastern spreading segment C. This
305 segment is characterized by a deep and narrow rift valley. Although thick sediment
306 makes it difficult to recognize magnetic anomalies in the eastern part of ABSC, this
307 segment is considered the oldest part of the ABSC [*Kamesh Raju et al.*, 2004]. The first
308 recorded event ($m_b=5.0$) of the swarm occurred about 15 km north of the ridge axis and
309 was immediately followed by two bigger events ($m_b=5.4$ and 5.3) located in the rift
310 valley. About 48 hours later, the main activity started in the rift valley and propagated
311 from the center of segment C southwestward along the ridge (Figure 8). The activity
312 persisted for more than a week, and a propagation velocity in the range of 0.2-0.6 km/h is
313 derived. A composite solution of the moment tensors in this swarm results in a NE-SW
314 striking normal fault with a marginal strike-slip component (Figure 7a) with the steeper
315 of the two double-couple planes dipping SE. Two mechanisms (O5, vPC1 in Figure 5, 7a,
316 and 8b) in the global CMT catalog deviate from the composite solution. Solution O5 has
317 a small strike-slip component and vPC1 falls in the category of vertical-P CLVD
318 mechanisms, which are mainly observed in volcanic regions and often interpreted as the

319 result of dip-slip motion on volcanic ring-faults [e.g., *Shuler et al.*, 2013]. We obtain a b-
320 value close to 2.0 (Figure S6) consistent with the result of *Mukhopadhyay and Dasgupta*
321 [2008].

322

323 A minor swarm occurred in August 1993 (green dots in Figure 7a) between segment A
324 and B, east of the 1973 swarm. The main activity only lasted for a few days (Figure S2)
325 and no CMT solutions are available for these events. The relocated epicenters spread over
326 a distance of about 20 km, clearly disconnected from and to the west of the 1984 swarm.

327

328 In March 2006, about 14 months after the December 2004 Mw=9.2 event, the largest of
329 the four swarms (Table 2), including ~130 events (yellow dots in Figure 7a), occurred at
330 the western edge of segment C and north of segment B. The swarm filled the spatial gap
331 between the 1984 and 1993 swarms. It initiated approximately at the WSW end of the
332 1984 swarm on ridge segment C and propagated southwestward along the ridge, similar
333 to the 1984 swarm but at much higher speed. Within two hours, the swarm events
334 covered a distance of about 50 kilometers along the ridge (Figure 8). After about eight
335 hours, seismic activity ceased in the rift valley of segment C. At the same time, intense
336 activity started off-axis north of segment B and lasted for about 2 days, before gradually
337 decaying over the following 20 days. The seafloor morphology in that area shows SW-
338 NE oriented lineaments and suggests fault scarps related to SE-dipping planes (Figure
339 7b). The composite moment tensor of this swarm corresponds to a NE-SW striking, pure
340 normal fault with the shallower of the two double-couple planes dipping SE. The b-value

341 of the 2006 swarm derived from mb reported in the ISC catalog is close to 2.0 (Figure
342 S6).

343

344 The 2009 swarm, while smaller (~50 events, Figure 7a), is similar to the 2006 swarm in
345 many aspects. The affected area and spatio-temporal evolution of the activity is similar to
346 the 2006 swarm, and the composite moment tensor is almost identical with the solution
347 derived from the 2006 earthquakes. The strike of CMT B-axes (indicated by thick lines in
348 Figure 7a) for several events in the 2006 and 2009 swarm align remarkably well with the
349 strike of the fault scarps seen in the bathymetry data north of segment B. Hypocenters
350 plotted in a vertical cross-section normal to the strike of these fault scarps reveal at least
351 two active faults that dip $\sim 30^\circ$ to the SE, consistent with the SE-dipping double-couple
352 planes (Figure 7b). The intersection of the projection of the shallower of the two faults
353 with the seafloor coincides with fault scarps seen in the bathymetry data. The b-value of
354 the 2009 swarm derived from mb reported in the ISC catalog is close to 2.0 (Figure S6).

355

356 **4. Discussion**

357 **4.1 Mode of extension in the Andaman Sea**

358 While formation of trench-parallel back-arc basins is commonly associated with trench
359 rollback, the oblique opening of the Andaman Sea (Figure 1) results from the
360 combination of two extensional components. *Curray* [2005] decomposed the average
361 spreading rates in the ABSC into a northward component (2.7 cm/yr) and a westward
362 component (1.2 cm/yr). The dominant northward component compares well with slip
363 rates observed along the Sumatra Fault [*Curray*, 2005], and its driving force seems to be

364 the northward dragging of the Burma sliver plate by the trench-parallel component of
365 convergence. Slip rates along the northern portion of the Sumatra Fault are on the order
366 of 2.7-2.5 cm/yr [*Sieh and Natawidjaja, 2000; Genrich et al., 2000*]. Present-day geodetic
367 slip rates along the Sagaing Fault in Myanmar are on the order of 1.8 cm/yr [*Vigny et al.,*
368 *2003; Maurin et al., 2010*] and therefore smaller than the average long-term northward
369 component of the spreading rate. This difference in slip rate can be explained by the
370 partitioning of motion between the India-Burma and Burma-Sunda plates and the slip
371 rates predicted by such a model agree to a first order with the observed rates [*Gahalaut*
372 *and Gahalaut, 2007*]. Northward motion might also be partially absorbed by diffuse fault
373 systems such as the extensional horsetail structure proposed by *Rangin et al. [1999]*
374 (Figure 1, 5, and 6). The smaller westward component of the spreading rate (1.2 cm/yr)
375 likely results from rollback, modulated by recurrent stresses due to coseismic slip and
376 afterslip on the plate interface.

377

378 The WAF system southeast of the ABSC seems to accommodate both dextral and
379 westward extensional motion (Figure 6), and the partitioning appears to be correlated in
380 time with coseismic slip and afterslip of the $M_w=9.2$ Sumatra-Andaman earthquake of
381 December 2004. Extensional mechanisms along the WAF system between 9.0°N and
382 10.5°N occur almost exclusively in the months after the 2004 earthquake (Figure 6) and
383 correlate in space with a peak in co- and postseismic deformation and moment release
384 [*Chlieh et al., 2007*]. This change from dextral towards extensional regime of the WAF
385 system was already noticed by others [e.g., *Engdahl et al., 2007; Cattin et al., 2009*],
386 however, whether or not extensional and strike-slip motion is partitioned on the same

387 fault (e.g. the WAF) cannot be answered conclusively. Based on bathymetry and
388 reflection seismic profiles [Curray, 2005; Kamesh Raju et al., 2007; Cochran, 2010], the
389 WAF is expected to dip steeply towards the east. In fact, fault planes associated with
390 dextral slip (such as C5, C6 in Figure 6) show dip angles of 80° to 90°. Fault planes
391 associated with eastward dipping normal faults (such as C7, C8 in Figure 6), however,
392 have shallower dip angles of 50° to 60°. The difference in fault dip suggests that the
393 extensional strain might be accommodated on splay structures of the master strike-slip
394 fault.

395

396 The inferred plate-boundary connecting the ABSC with the Sagaing Fault consists of a
397 right-lateral transform with prominent extensional bends (solid black line within dashed
398 region in Figure 6). The contribution to overall back-arc extension, as indicated by the
399 distribution of extensional CMT solutions and seismic moment (Table 1, Figure 6), seems
400 minor. A large fraction of the seismic moment release in this region is accommodated by
401 oblique-slip mechanisms (Table 1) suggesting the presence of young structures, where
402 strain partitioning is not yet developed. Normal-fault earthquakes, as observed in cluster
403 C1 and C2 (Figure 4b and 6), accommodate additional extension at the eastern edge of
404 the Alcock Rise on NE-SW striking faults [see also Rangin et al., 1999; Curray, 2005].
405 These faults consistently locate west of the inferred plate boundary that hosts the strike-
406 slip events (Figure 4b and 6). The spatio-temporal evolution of these earthquakes, and the
407 fact that the normal faulting events closest to the transform fault have a significant strike-
408 slip component (Figure 4b), suggest that the extensional events accommodate additional
409 bending related residual stresses from slip on the east veering transform plate boundary in

410 that region. The NW-SE orientation of T-axes of the extensional earthquakes N2-N8 in
411 Figure 4b agrees with the T-axes orientation observed for the two nearby strike-slip
412 events S1-S2 and is similar to the general trend of the ABSC (Figure 6).

413

414 Seafloor morphology and the orientation of relocated seismicity in combination with the
415 strike of right-lateral fault planes such as S1-S3 suggest that the inferred transform fault
416 (solid black line within dashed region in Figure 6) links the ABSC with the short
417 spreading segment of cluster C3 (Figure 4b, 5, and 6). Earthquake swarms in 1983 and
418 1984 in cluster C3 are indicative of active spreading processes involved in the formation
419 of this basin. Three available moment tensor solutions (O1-O3, Figure 4d), however,
420 indicate oblique slip. Oblique slip likely contributes to the basin development similar to
421 transtensional mechanisms proposed for basin formation in the Marmara Sea [*Seeber et*
422 *al.*, 2006].

423

424 Seismicity is more diffuse between the short spreading segment of cluster C3 and the
425 Sagaing Fault (Figure 5 and 6) and no clear connection between both structures is
426 resolved. *Chamot-Rooke et al.* [2001] proposed an eastward connection of the short
427 spreading segment of cluster C3 to a series of grabens, forming the horsetail termination
428 of the Sagaing Fault system (Figure 5 and 6). The strike of right-lateral fault planes such
429 as of O2-O4 and S4 (Figure 5), however, deviates significantly from the general WSW-
430 ENE strike of the proposed horsetail system. Well-constrained hypocenters in the EHB
431 catalog report focal depths in the range of 14-25 km for these events (Figure 5), which
432 places them in the lower part of the crust. Relocated seismicity is concentrated along a

433 band in the western end of the horsetail system (Figure 6). Therefore we cannot rule out a
434 possible connection to the Sagaing Fault by a system of faults in the underlying basement
435 (outlined by gray shaded area in Figure 6).

436

437 The distribution of extensional CMT solutions and seismic moment in the Andaman Sea
438 suggests that back-arc extension occurs primarily in the ABSC (Table 1, Figure 6). To
439 quantify the direction and the amount of extension accommodated by seismic slip on
440 normal-faults in the ABSC, we calculated the short-term spreading rate by following the
441 calculations of *Guzman-Speziale and Ni* [1993] with modified model assumptions and
442 updated global CMT solutions. The direction of maximum extensive strain is defined by
443 the eigenvector e_l associated with the largest eigenvalue λ_l of the summed moment
444 tensor \underline{M}_s of all normal-faulting events at the ridge. The spreading rate v can be derived
445 from:

$$446 \quad v = \frac{1}{2\mu\tau Lh} \lambda_l, \quad (1)$$

447 with τ being the time interval, μ the shear modulus ($3 \cdot 10^{10}$ N/m²), L the length of the
448 ridge, h the maximum depth of the seismogenic layer, and λ_l the largest eigenvalue of
449 \underline{M}_s . We assume that recent and current extension correlates with normal-fault earthquakes
450 along segment C and B of the ABSC and L is about 84 km (Figure 7a). The cross-section
451 in Figure 7b suggests a seismogenic layer of about 18 km, however, these events are off-
452 axis and represent reactivation of existing faults. Instead, we use a seismogenic layer h of
453 10 km, a value commonly assumed to be the maximum focal depth at mid-ocean rifts
454 [*Huang and Solomon*, 1988]. Because the actual depth of the seismogenic layer lies

455 somewhere between 10 and 18 km, the spreading rate derived from equation 1 with $h =$
456 10 km should only be considered as an upper bound rather than a best estimate. We sum-
457 up all CMT solutions with P-axes plunging $\geq 60^\circ$ (normal-faulting type). We find 57 of
458 these events between 1984 and 2009 ($\tau=26$ yr). The largest eigenvalue λ_1 of $\underline{\mathbf{M}}_s$ is
459 $3.301 \cdot 10^{18}$ Nm. The direction of maximum extensive strain defined by eigenvector \mathbf{e}_1 is
460 N22°W, which is close to the value of N19°W found by *Guzman-Speziale and Ni* [1993].
461 It also compares well to the long-term spreading direction of N25°W derived by *Curray*
462 [2005] from reconstruction of the ABSC over the past 4 Myr. Using equation 1, the
463 maximum bound on the tectonic contribution to the spreading rate v of our model is about
464 0.25 cm/yr, which is about five times higher than what *Guzman-Speziale and Ni* [1993]
465 obtain (0.05 cm/yr), but more than one order of magnitude smaller than the long-term
466 opening rate of 3.0-3.8 cm/yr [*Kamesh Raju et al.*, 2004; *Curray* 2005]. Since the 1984
467 and 2009 swarms bracket the observation period, τ might also be underestimated. Thus,
468 seismic-slip on normal faults accounts at most for 7-8% of the long-term opening rate.
469 Similar to *Guzman-Speziale and Ni* [1993] and *Solomon et al.* [1988], we interpret the
470 deficit in seismically accommodated extension as indication for aseismic processes. The
471 deficit in seismic moment and the morphology of the ABSC supports an active spreading
472 system, where extension (driven by far field forces) is largely accommodated by intrusion
473 of new crust along the central neovolcanic zone. The proposed formation of new crust is
474 further supported by magnetic anomalies from shipboard surveys [*Kamesh Raju et al.*,
475 2004] and satellite data (Figure S9). Recent industry seismic reflection data image many
476 sills below the basement, also indicative for ongoing dike and intrusion processes
477 [*Singh et al.*, 2010]. The thick sedimentary cover of the northeastern ridge segment likely

478 acts as a blanket for volcanic eruptions and hydrothermal circulation, suggesting an
479 accretionary process different from typical oceanic spreading [*Singh et al.*, 2010].

480

481 **4.2 Structure and fault geometry of the ABSC**

482 Similar to slow-spreading ridges in the Mid-Atlantic, the morphology of the ABSC is
483 characterized by a distinct rift valley bounded by a series of scarps and steplike terraces,
484 which are apparent in the high-resolution bathymetry maps on either side of the rift
485 (Figure 7a and 8) and in cross-axis bathymetry profiles (Figure 9). We interpret these
486 fault scarps as expressions of inward facing normal faults. These faults are indicative of
487 tectonic extension processes (including faulting, uplifting, and tilting of blocks) and may
488 contribute significantly to the formation of the axial depression of slow-spreading ridges
489 [e.g., *Mutter and Karson*, 1992]. Fault scarps in the inside corners of segment B and C
490 appear to have larger throws than elsewhere along the ABSC (Figure 9).

491

492 The role of inward-facing normal faults in the architecture of the rift valley is confirmed
493 by two single channel seismic reflection profiles, penetrating the first few kilometers of
494 the crust (Fig. 10 of *Kamesh Raju et al.* [2004]). A profile across segment C (close to
495 profile 20 of Figure 9 and 10a), suggests a full graben structure. It images inward facing
496 normal faults with corresponding fault scarps in the bathymetric cross-section of profile
497 20 and 21 (Figure 9). A second seismic profile close to DD' of Figure 7b across segment
498 B indicates inward facing normal faults southeast of the rift valley. To the northwest
499 *Kamesh Raju et al.* [2004] interpret near seafloor reflections as shallow basement,
500 however, faults are not resolved in this part of the seismic image.

501

502 Seismicity along profile DD' suggests moderately dipping faults north of segment B
503 (Figure 7b). In contrast, seismicity profiles across segment C provide no constraint on
504 fault dip. Insufficient depth resolution of hypocenters due to fewer and lower quality data
505 in 1984 may be a factor, in addition to possible along-strike discontinuities between
506 faults. Information on fault dips across segment C is derived from CMT double-couple
507 solutions. The preferred fault planes are inward facing, following observations from the
508 two seismic profiles and the seismicity profile DD'. We choose southward dipping fault
509 planes for earthquakes that locate northwest of the ridge axis and northward dipping
510 planes for earthquakes located southwest of the axis. We do not consider events located
511 in the offset area between segment B and C, due to the lack of information on fault dip
512 direction in this area. Our preferred fault planes are shown as gray arrows in Figure 7a,
513 representing projections of slip vectors calculated from strike, dip, and rake of the
514 preferred double-couple solution. Steeply dipping faults (50° - 75°) occur preferentially in
515 the central part of segment C, where they are likely associated with the main boundary
516 faults of the inner floor of the rift valley. Similar mechanisms were proposed for the
517 largest earthquakes on the Mid-Atlantic ridge [e.g., *Bergman and Solomon*, 1990]. The
518 moderately dipping fault planes (27° - 45°) north of segment B (Figure 10b) are consistent
519 with the dip of the proposed off-axis faults observed along profile DD' in Figure 7b.

520

521 The offset between segments C and B is small, ~ 13 km, and appears to be a non-
522 transform discontinuity (Figure 7a and 9). It subdivides the deep, distinct, narrow valley
523 in segment C from the shallow, rugged depression in segment B (Figure 9). Similar non-

524 transform discontinuities are found in parts of the Mid-Atlantic Ridge [e.g., *Sempere et*
525 *al.*, 1990], where they are associated with lateral differences in the magma supply [e.g.,
526 *Macdonald et al.*, 1991]. Alternative models propose mechanical deformation to explain
527 segmentation at slow-spreading ridges [e.g., *Mutter and Karson*, 1992]. Prominent
528 expressions of mechanical deformation are oceanic detachments at inside corners of jogs
529 along slow-spreading ridges [e.g., *Tucholke and Lin*, 1994; *Escartin et al.*, 2008]. The
530 spatial correlation between large-offset faults and ridge-discontinuities in the ABSC
531 (Figure 9) suggests the involvement of mechanical processes, even though fault scarps
532 north of segment B are quite different from typical oceanic detachments. Whether or not
533 the offset between C and B is of ‘magmatic’ or ‘mechanical’ origin remains unclear. On a
534 broader scale, ridge segmentation is typical of oblique spreading systems dominated by
535 remote tectonic stresses [e.g., *Abelson and Agnon*, 1997] and might indicate a re-
536 adjustment of the ridge as discussed later.

537

538 The ABSC displays many of the key features of mid-ocean ridges, yet, some differences
539 are noteworthy. In contrast to mid-ocean ridges, the transform and non-transform
540 discontinuities at the ends of segment C coincide with minimum axial depths. Also,
541 segment C does not exhibit the typical axial high (Figure 9), but thick sediment masks
542 basement morphology along this segment. The ABSC is unusual among spreading ridges
543 in being surrounded by sediment sources and thus receiving not only high, but also
544 spatially variable sedimentation. Changes in sediment cover accounts for some of the
545 differences in sea floor morphology along the ABSC [*Kamesh Raju et al.*, 2004; *Curray*,
546 2005; *Singh et al.*, 2010], but may also account for structural differences. In models

547 proposed for rifting in the Gulf of California deposition of sediments promotes narrow
548 rifting [*Lizarralde et al.*, 2007; *Bialas and Buck*, 2009]. Accordingly, the thick sediment
549 cover deposited by turbidity currents that are reaching segment C, but not B, may have
550 led to the observed along-axis difference in the extensional styles between these
551 segments.

552

553 **4.3 Kinematics of the ABSC**

554 Although some earthquakes in the 1984 sequence are off-axis, the main activity within
555 this swarm concentrates beneath the rift valley on steeply dipping faults (Figures 7a and
556 10b). The seismic activity propagates over 40 km along the rift from ENE to WSW
557 (Figure 8b) with a velocity of about 0.6 km/h, comparable to propagation velocities
558 observed in other rift systems (Iceland: 1.8 km/h [e.g., *Einarsson and Brandsdottir*,
559 1980]; Afar: 1.1 km/h [e.g., *Ayele et al.*, 2009]). Swarms associated with seafloor
560 spreading events along the Juan de Fuca and Gorda ridge in the Eastern Pacific show
561 very similar migration rates of 0.2 to 2.0 km/h [*Dziak et al.*, 2007]. Magmatic processes
562 are predicted by the deficit in seismic moment, high b-values, the presence of seafloor
563 spreading magnetic anomalies [*Kamesh Raju et al.*, 2004], as well as by seismic
564 reflection data of *Singh et al.* [2010]. Therefore we interpret the 1984 swarm as
565 expression of a dike intrusion propagating laterally towards WSW. The occurrence of
566 exclusively normal-faulting events on the main boundary faults of the inner rift floor is
567 consistent with volcanic-spreading events on mid-ocean ridges [e.g., *Tolstoy et al.*, 2001]
568 and can be accounted for by the tensile stress field that forms above the propagating dike
569 [*Rubin*, 1992]. The location of the vertical-P CLVD mechanisms vPC1 in the 1984

570 swarm coincides with the oblique mechanism O5 (Figure 7a). Event O5 occurred on 8
571 July (05:26) followed by event vPC1 about 11 hours later (Figure 8b). As proposed by
572 *Ekström* [1994], such vertical-CLVD mechanism can be explained by dip-slip motion on
573 volcanic ring-faults. *Shuler et al.* [2013] found a strong correlation between the
574 occurrence of vertical-CLVD mechanisms and volcanic unrest, where vertical-P
575 mechanisms generally occur after eruptions. The location and timing of event O5 and
576 vPC1 might therefore be indicative for volcanic processes such as deflating or collapse of
577 a magma chamber in the center of segment C during the swarm.

578

579 In contrast to the 1984 sequence, earthquakes within the 2006 swarm occurred nearly
580 concurrently (within two hours) over more than 50 km across the western part of segment
581 C beneath the rift valley, followed by an increased seismic activity in the fault scarp
582 region north of segment B (Figure 8). If there were a propagation, it would have
583 velocities >20 km/h, much higher than known lateral dike propagation velocities. The
584 instantaneous occurrence of earthquakes is better explained as the consequence of near-
585 simultaneous injections vertically from an axial magma lens, as proposed by *Dziak et al.*
586 [2009]. Studies by *Cattin et al.* [2009] and *Sevilgen et al.* [2012] suggest that a critical
587 stress regime may have built up in the back-arc due to the December 2004 $M_w=9.2$
588 earthquake. Stress calculations show that the megathrust rupture increased the Coulomb
589 stress on normal faults within the ABSC region. The Coulomb stress increase in the
590 ABSC derived by *Cattin et al.* [2009] and *Sevilgen et al.* [2012], however, is very small
591 (about 0.2-0.3 bar) and does not explain the lag of 14 months between the 2004 rupture
592 and the 2006 swarm.

593

594 In order to compare the amplitudes of the post-2004 regional stress change to local
595 stresses resulting from a dike intrusion, we modeled the Coulomb stress change due to a
596 hypothetical tensile dike opening at the location of the 2006 earthquake swarm using the
597 COULOMB software package [Stein, 1999]. The modeled dike assumes a typical
598 opening of 1 m and a height of 1.5 km [e.g., Buck *et al.*, 2006; Dziak *et al.*, 2009]. The
599 along-strike extent of the modeled dike beneath segment C is derived from the
600 distribution of hypocenters within the first 4 hours of the 2006 swarm and it is shown as a
601 solid white line in Figure 8a. Its vertical position is based on seismic reflection profiles
602 [Singh *et al.*, 2010] and ranges from 4.0 km to 5.5 km depth (from seabed). The average
603 positive Coulomb stress change on axial normal faults (receiver fault: strike = 73°, dip =
604 58°, rake = -92°) above (and below) the opening dike at profile G in Figure 8a (depth
605 range 0-20 km) is 3.6 bar. This value significantly exceeds possible coseismic stress
606 perturbations that may have originated from the Dec. 2004 rupture in the ABSC. Dike
607 opening also leads to positive Coulomb stress changes on the proposed moderately
608 dipping normal faults (receiver fault: strike = 63°, dip = 36°, rake = -96°) in the off-axis
609 region. The average positive Coulomb stress change at the location of profile F in Figure
610 8a (depth range 0-20 km) is 0.4 bar, comparable to coseismic stress perturbations
611 predicted by Cattin *et al.* [2009] and Sevilgen *et al.* [2012] for the December 2004
612 Mw=9.2 earthquake. As shown in section S.6 of the electronic supplement, the overall
613 results are rather independent of the details of the chosen dike geometry.

614

615 Based on the above we argue that the primary driver for the 2006 swarm was a magmatic
616 intrusion, probably vertically injected from an axial magma lens beneath the WSW part
617 of segment C. Earthquakes on moderately dipping off-axis faults may have been
618 triggered by stress changes from the magmatic intrusion as well as from the primary
619 sequences of earthquakes on axial faults in the rift valley along segment C. Similarities in
620 location, b-values, and the spatio-temporal behavior of seismicity suggest a similar
621 mechanism for the 2009 swarm, although the propagation velocity in the 2009 swarm (on
622 the order of a few kilometers per hour) appears lower than in the 2006 sequence and
623 somewhat closer to values typically associated with lateral dike intrusion. Aseismic
624 opening of the Andaman Sea at a rate of 3.8 cm/yr would require dike injections about
625 every 25 years (assuming a typical dike thickness of ~1 m), which is roughly consistent
626 with the period between the 1984 and the 2006/2009 swarms. No additional swarm was
627 identified in the ISC catalog between 1964 and 1984 along segment C. Differences in the
628 apparent migration rates of the three swarms, however, seem to hint that properties of
629 injections such as dike width might not be uniform and that there is not a simple
630 horizontal propagation but a combination of horizontal propagation and vertical
631 injections. The westward propagation of dike intrusions and the potentially vertical
632 injection during the 2006 event also implies the existence of several magma lenses
633 beneath segment C, rather than one magma supply in the center of the segment. The
634 WSW propagation of the swarms as well as the seismic activity within each swarm, on
635 the other hand, suggest an ‘unzipping’ of segment C from ENE to WSW, consistent with
636 the proposed long-term westward propagation of the spreading center [*Kamesh Raju et*
637 *al.*, 2004]. Whether or not the 2006/2009 intrusion events have been triggered by the

638 2004 Mw=9.2 Sumatra-Andaman earthquake remains unclear. Volumetric expansion in
639 the back-arc region due to the megathrust earthquake as proposed by *Walter and*
640 *Amelung* [2007] in combination with fluid-diffusion processes might be mechanisms to
641 explain the delay of 14 months.

642

643 **4.4 Strain partitioning in a non-orthogonal ridge-transform system**

644 The net long-term spreading direction in the ABSC is about N25°W [*Curray*, 2005] and
645 therefore nearly normal to the general trend of the ridge, but oblique to the adjacent
646 transforms, as illustrated by the conceptual end-member model displayed in Figure 11a.
647 To study how and to which degree strain is partitioned within such a non-orthogonal
648 system, we begin with a detailed analysis of nodal planes and slip vectors from global
649 CMT solutions in the ABSC. In Figure 10c and 10d we plot strike and rake of the
650 preferred (inward dipping) double-couple nodal planes with respect to their position
651 along the ridge. For solutions without preferred planes (events in the overlapping zone
652 between segment C and B) we plot the directions of B-axes instead of fault strike (gray
653 dots in Figure 10c).

654

655 Nodal planes along segment C suggest clockwise misalignment with respect to the ridge
656 axis (shown as solid line in Figure 10c), with deviations up to 25°. The median strike of
657 preferred planes and directions of B-axes along segment C is 73°, which corresponds to a
658 deviation of 8° from ridge-parallel as shown by the rose diagram in Figure 10c. The
659 direction of the principle tensile strain derived from the composite moment tensor of

660 CMT solutions along segment C (shown as dashed-dotted line in Figure 10c) indicates a
661 similar clockwise deviation of about 6° from ridge-normal.

662

663 To the WSW, fault strike of earthquakes in the fault scarp region and along segment B
664 appear to align with the strike of segment B (median strike of preferred planes between
665 106 and 130 km in Figure 10c is 60°) and the inferred tension direction is close to normal
666 to the ridge axis (Figure 6, 7a and 10c). Two solutions, however, are anti-clockwise
667 misaligned. No CMT solutions are available for earthquakes located at spreading segment
668 A.

669

670 The rakes of preferred nodal planes distribute around -90° (Figure 10d) indicating pure
671 dip-slip normal faulting. A systematic shift towards minor dextral components of slip
672 vectors is apparent in the fault scarp region (rake about -105°). Few individual solutions
673 along the ridge indicate larger deviation from pure dip-slip mechanisms (rake of about -
674 120° and -60° respectively).

675

676 The conceptual model of Figure 11a agrees well with the general characteristics of the
677 ABSC. However, while the spreading direction (*SD* in Figure 11) is perfectly normal to
678 the strike of segment C, it is slightly oblique to segments A, B, and the general trend of
679 the ridge axis (Figure 11b). The angle between the spreading direction and the normal to
680 the general trend of the ridge axis is only about 6° , much smaller than values typically
681 considered as oblique spreading [e.g., *Abelson and Agnon, 1997*]. Thus, we conclude that
682 dip-slip normal faulting and the $N22^\circ W$ direction of maximum extensive strain of the

683 cumulative CMT solution along the ridge are consistent with ridge-normal spreading. The
684 N-S oriented troughs on either end of the ABSC (Figure 5 and 6) might be expressions of
685 the ‘leaky’ character of the adjacent transforms, due to westward extension across the
686 strike-slip faults [e.g., *Menard and Atwater, 1968; Thompson and Melson, 1972; Taylor*
687 *et al., 1994*].

688

689 As illustrated in Figure 11b, the ridge is fragmented into three discordant segments
690 obliquely oriented to its general trend. Such (second order) ridge segmentation is
691 predicted by the crack model of *Abelson and Agnon [1997]* for oblique spreading systems
692 dominated by remote tectonic stresses. The possible clockwise deviation of fault strike
693 (*SC*) from the maximum extensive strain (*TC*) and the spreading direction (*SD*) along
694 segment C (Figure 10c and 11b) suggests that the horizontal principal compressive stress
695 axes ($S_H > S_h$) are oblique to both the spreading direction and the trend of the ridge,
696 consistent with the ‘transtensional’ model of *Tuckwell et al. [1996]*. In their model,
697 extensional fractures and normal faults form normal to the minimum principal
698 compressive stress S_h but oblique to ridge and plate vector. The extensional faults and
699 dikes may form en-echelon arrays along the ridge axis. Thus, the observed misalignment
700 of our nodal planes might indicate a similar en-echelon arrangement of dikes along
701 segment C. But the observed 8° deviation of the median fault strike from ridge-parallel
702 along segment C might not be resolvable. Differences of 5-7° between moment tensors
703 can be introduced by approximations in the modeling [e.g., *Hjörleifsdóttir and Ekström,*
704 *2010*] and studies comparing source parameters of different catalogs report uncertainties
705 of 5-7° in moment tensors for the best CMT solutions [*Kagan, 2003*]. Based on a similar

706 study, *Helffrich* [1997] concluded that the slip-vector uncertainty of a typical shallow
707 earthquake is 14° . It is unlikely, however, that uncertainties in the moment tensor or slip
708 vector are solely assigned to the fault-strike component. The rather good agreement
709 between fault strike and ridge orientation along segment B suggests that the observed
710 misalignment along C is consistent with the overall discordant orientation of ridge segment
711 B and C.

712

713 Whether or not such non-orthogonal ridge-transform systems represent stable
714 configurations over time or adjust towards orthogonal geometries remains controversial
715 [e.g., *Lachenbruch and Thompson*, 1972; *Lachenbruch*, 1976; *Atwater and Macdonald*,
716 1977; *Tanaka and Fujii*, 1991]. In the Andaman Sea, structures are in place to lock
717 geometry and direction of spreading. For instance, the position and geometry of
718 transforms in the ABSC-system seem to be controlled by plateaus like the Alcock Rise,
719 where the plate boundary follows the shape of its eastern edge (Figure 6). The initial NE-
720 SW orientation of the spreading ridge is probably reflecting pre-existing structures within
721 these plateaus, similar to normal faults imaged by clusters C1 and C2. The clockwise
722 deviation of ridge segment A and C from the general trend of the ridge as well as possible
723 clockwise deviation of fault strike and maximum extensive strain along segment C
724 suggest that the segment geometry is not in equilibrium with current plate-motion
725 demands and thus indicate ongoing re-adjustment of the ridge. Reorientation might occur
726 by rift propagation [e.g., *Hey et al.*, 1988], for instance along segment C, which seems to
727 be the most appropriately oriented ridge segment for the current spreading demands.

728 Such a rift propagation concept would be consistent with the concentration of
729 earthquakes beyond the SW end of segment C and the WSW migration of swarms.

730

731 **5. Conclusions**

732 Teleseismic cross-correlation based double-difference relocation of seismicity in the
733 Andaman Sea reveals insight into the spatial and temporal structure and dynamics of this
734 extensional plate boundary system. The new data image NE-SW trending active normal
735 faults at the eastern edge of the Alcock Rise, which accommodate the NW-SE directed
736 extension in the Andaman Sea. These normal faults are located west of the master plate
737 boundary, which is inferred from N-S trending transform faults connecting the Andaman
738 Back-Arc Spreading Center (ABSC) with the Sagaing Fault. Seismicity and seismic
739 moment release suggest that back-arc extension is primarily accommodated within the
740 ABSC. However, the short-term spreading rate derived from extensional moment tensors
741 account for less than 10% of the long-term 3.0-3.8 cm/yr spreading rate. The deficit in
742 seismic strain supports the concept of a spreading system, where extension is largely
743 accommodated by formation of new crust.

744

745 Episodes of dike intrusions are proposed as the primary driver for three major earthquake
746 swarms in the ABSC. Directivity and migration velocities of seismicity in the 1984
747 swarm are interpreted as expression of a tensile stress field that forms above a lateral dike
748 intrusion initiated in the central part of segment C, propagating towards WSW. High b -
749 values of about 2 and the occurrence of a potential vertical-CLVD mechanism in the
750 center of segment C are additional hints for a magmatic origin of the 1984 swarm.

751 Swarms in 2006 and 2009 initiated at the WSW end of segment C and show similar
752 propagation towards WSW. Coulomb-stress modeling suggests that dike-opening and
753 axial earthquakes triggered seismic activity on moderately inward-dipping off-axis faults
754 north of segment B. The period of about 25 years between the 1984 and 2006/2009
755 swarms is consistent with the long-term spreading rate of 3.8 cm/yr (assuming a dike
756 thickness of 1 m and purely aseismic opening).

757

758 The spreading direction in the ABSC over the past 4 Myr appears to be close to ridge
759 normal, but oblique to the adjacent transforms. The non-orthogonal ridge-transform
760 geometry results in the formation of ‘leaky transforms’, consistent with NS oriented deep
761 troughs evident in the bathymetry on either side of the ABSC. In particular, the West
762 Andaman Fault system accommodates westward extension in the month after the
763 Mw=9.2 Sumatra-Andaman earthquake of December 2004. A possible systematic skew
764 in slip vectors suggests an en-echelon arrangement of extensional structures in the eastern
765 part of the ABSC, which indicates that segment geometry is not in equilibrium with
766 current plate-motion demands and thus ongoing re-adjustment of the ridge.

767

768 **Acknowledgements**

769 We thank Roger Buck, Göran Ekström, and Jochen Wössner for helpful discussions.
770 Comments by the associate editor, Frederik Tilmann, and two anonymous reviewers
771 helped to improved the manuscript. This work was supported in part by the National
772 Science Foundation under grants EAR-06-08739 (T.D., F.W., E.R.E.) and OCE-0927024
773 (T.D., J.C., F.W., K.K.-R.). LDEO contribution number XXXX. Seismic waveform data

774 were obtained from the Incorporated Research Institutions for Seismology (IRIS) and the
775 GEOFON data center. The bulletin data were provided by the ISC and USGS/NEIC and
776 moment tensor solutions were obtained from the Global CMT Project. Figures were
777 prepared using the GMT software package [*Wessel and Smith, 1998*].

778

778

References

779 Abelson, M., and A. Agnon (1997), Mechanics of oblique spreading and ridge
780 segmentation, *Earth Planet Sci. Lett.*, 148(3-4), 405-421.

781 Atwater, T., and K. C. Macdonald (1977), Are spreading centers perpendicular to their
782 transform faults?, *Nature*, 270(5639), 715-717.

783 Ayele, A., D. Keir, C. Ebinger, T. J. Wright, G. W. Stuart, W. R. Buck, E. Jacques, G.
784 Ogubazghi, and J. Sholan (2009), September 2005 mega-dike emplacement in the
785 Manda-Harraro nascent oceanic rift (Afar depression), *Geophys. Res. Lett.*, 36, L20306.

786 Bergman, E. A., and S. C. Solomon (1990), Earthquake swarms on the Mid-Atlantic
787 Ridge - products of magmatism or extensional tectonics?, *J. Geophys. Res.*, 95(B4),
788 4943-4965.

789 Bialas, R. W., and W. R. Buck (2009), How sediment promotes narrow rifting:
790 application to the Gulf of California, *Tectonics*, 28.

791 Briggs, R. W., K. Sieh, A. J. Meltzner, D. Natawidjaja, J. Galetzka, B. Suwargadi, Y. J.
792 Hsu, M. Simons, N. Hananto, I. Suprihanto, D. Prayudi, J. P. Avouac, L. Prawirodirdjo,
793 and Y. Bock (2006), Deformation and slip along the Sunda Megathrust in the great 2005
794 Nias-Simeulue earthquake, *Science*, 311(5769), 1897-1901.

795 Buck, W. R., P. Einarsson, and B. Brandsdottir (2006), Tectonic stress and magma
796 chamber size as controls on dike propagation: constraints from the 1975-1984 Krafla
797 rifting episode, *J. Geophys. Res.*, 111(B12).

798 Cattin, R., N. Chamot-Rooke, M. Pubellier, A. Rabaute, M. Delescluse, C. Vigny, L.
799 Fleitout, and P. Dubernet (2009), Stress change and effective friction coefficient along
800 the Sumatra-Andaman-Sagaing fault system after the 26 December 2004 (Mw=9.2) and
801 the 28 March 2005 (Mw=8.7) earthquakes, *Geochem. Geophys. Geosy.*, 10, Q03011,
802 doi:10.1029/2008GC002167.

803 Chamot-Rooke, N., C. Rangin, and C. Nielsen (2001), Timing and Kinematics of
804 Andaman basin opening, paper presented at AGU Spring Meeting, Abstract T42B-08.

805 Chlieh, M., J. P. Avouac, V. Hjorleifsdottir, T. R. A. Song, C. Ji, K. Sieh, A. Sladen, H.
806 Hebert, L. Prawirodirdjo, Y. Bock, and J. Galetzka (2007), Coseismic slip and afterslip of
807 the great Mw 9.15 Sumatra-Andaman earthquake of 2004, *Bull. Seismol. Soc. Am.*, 97(1),
808 S152-S173.

809 Cochran, J. R. (2010), Morphology and tectonics of the Andaman Forearc, northeastern
810 Indian Ocean, *Geophys. J. Int.*, 182(2), 631-651.

811 Curray, J. R. (2005), Tectonics and history of the Andaman Sea region, *J. Asian Earth*
812 *Sci.*, 25(1), 187-228.

813 Curray, J. R., D. G. Moore, L. A. Lawver, F. J. Emmel, R. W. Raitt, M. Henry, and R.
814 Kieckhefer (1979), Tectonics of the Andaman Sea and Burma, in *Geological and*
815 *Geophysical Investigations of Continental Margins*, edited by J. Watkins, L. Montadert
816 and P. W. Dickerson, pp. 189-198, Am. Assoc. Pet. Geol. Mem. 29.

817 Dick, H. J. B., J. Lin, and H. Schouten (2003), An ultraslow-spreading class of ocean
818 ridge, *Nature*, 426(6965), 405-412.

819 Dziak, R. P., D. R. Bohnenstiehl, J. P. Cowen, E. T. Baker, K. H. Rubin, J. H. Haxel, and
820 M. J. Fowler (2007), Rapid dike emplacement leads to eruptions and hydrothermal plume
821 release during seafloor spreading events, *Geology*, 35(7), 579-582.

822 Dziak, R. P., D. R. Bohnenstiehl, H. Matsumoto, M. J. Fowler, J. H. Haxel, M. Tolstoy,
823 and F. Waldhauser (2009), January 2006 seafloor-spreading event at 9 degrees 50 ' N,
824 East Pacific Rise: Ridge dike intrusion and transform fault interactions from regional
825 hydroacoustic data, *Geochem. Geophys. Geosy.*, 10, Q06T06,
826 doi:10.1029/2009GC002388.

827 Eguchi, T., S. Uyeda, and T. Maki (1979), Seismotectonics and tectonic history of the
828 Andaman Sea, *Tectonophysics*, 57(1), 35-51.

829 Einarsson, P., and B. Brandsdottir (1980), Seismological evidence for lateral magma
830 intrusion during the July 1978 deflation of the Krafla volcano in Ne Iceland, *Journal of*
831 *Geophysics*, 47(1-3), 160-165.

832 Ekström, G. (1994), Anomalous earthquakes on volcano ring-fault structures, *Earth*
833 *Planet. Sci. Lett.*, 128, 707-712.

834 Engdahl, E. R., R. van der Hilst, and R. Buland (1998), Global teleseismic earthquake
835 relocation with improved travel times and procedures for depth determination, *Bull.*
836 *Seismol. Soc. Am.*, 88(3), 722-743.

837 Engdahl, E. R., A. Villasenor, H. R. DeShon, and C. H. Thurber (2007), Teleseismic
838 relocation and assessment of seismicity (1918-2005) in the region of the 2004 Mw 9.0
839 Sumatra-Andaman and 2005 Mw 8.6 Nias Island great earthquakes, *Bull. Seismol. Soc.
840 Am.*, 97(1), S43-S61.

841 Escartin, J., D. K. Smith, J. Cann, H. Schouten, C. H. Langmuir, and S. Escrig (2008),
842 Central role of detachment faults in accretion of slow-spreading oceanic lithosphere,
843 *Nature*, 455(7214), 790-795.

844 Fitch, T. J. (1972), Plate convergence, transcurrent faults, and internal deformation
845 adjacent to southeast Asia and western Pacific, *J. Geophys. Res.*, 77(23), 4432-4460.

846 Gahalaut, V. K., and K. Gahalaut (2007), Burma plate motion, *J. Geophys. Res.*,
847 112(B10), doi:10.1029/2007JB004928.

848 Genrich, J. F., Y. Bock, R. McCaffrey, L. Prawirodirdjo, C. W. Stevens, S. S. O.
849 Puntodewo, C. Subarya, and S. Wdowinski (2000), Distribution of slip at the northern
850 Sumatran fault system, *J. Geophys. Res.*, 105(B12), 28327-28341.

851 Guzman-Speziale, M., and J. F. Ni (1993), The opening of the Andaman Sea - where is
852 the short-term displacement being taken up?, *Geophys. Res. Lett.*, 20(24), 2949-2952.

853 Helffrich, G. R. (1997), How good are routinely determined focal mechanisms?
854 Empirical statistics based on a comparison of Harvard, USGS and ERI moment tensors,
855 *Geophys. J. Int.*, 131(3), 741-750.

856 Hey, R. N., H. W. Menard, T. M. Atwater, and D. W. Caress (1988), Changes in
857 direction of seafloor spreading revisited, *J. Geophys. Res.*, 93(B4), 2803-2811.

858 Hjörleifsdóttir, V., and G. Ekström (2010), Effects of three-dimensional Earth structure
859 on CMT earthquake parameters, *Phys. Earth Planet. In.*, 179(3-4), 178-190.

860 Huang, P. Y., and S. C. Solomon (1988), Centroid Depths of Mid-Ocean Ridge
861 Earthquakes - Dependence on Spreading Rate, *J. Geophys. Res.*, 93(B11), 13445-13477.

862 Kagan, Y. Y. (2003), Accuracy of modern global earthquake catalogs, *Phys. Earth*
863 *Planet. In.*, 135(2-3), 173-209.

864 Kamesh Raju, K. A., G. P. S. Murty, D. Amarnath, and M. L. M. Kumar (2007), The
865 west Andaman fault and its influence on the aftershock pattern of the recent megathrust
866 earthquakes in the Andaman-Sumatra region, *Geophys. Res. Lett.*, 34(3), L03305,
867 doi:10.1029/2006GL028730.

868 Kamesh Raju, K. A., T. Ramprasad, P. S. Rao, B. R. Rao, and J. Varghese (2004), New
869 insights into the tectonic evolution of the Andaman basin, northeast Indian Ocean, *Earth*
870 *Planet Sci. Lett.*, 221(1-4), 145-162.

871 Kundu, B., D. Legrand, K. Gahalaut, V. K. Gahalaut, P. Mahesh, K. A. Kamesh Raju, J.
872 K. Catherine, A. Ambikapthy, and R. K. Chadha (2012), The 2005 volcano-tectonic
873 earthquake swarm in the Andaman Sea: Triggered by the 2004 great Sumatra-Andaman
874 earthquake, *Tectonics*, 31, TC5009, doi:10.1029/2012TC003138.

875 Lachenbruch, A. H. (1976), Dynamics of a passive spreading center, *J. Geophys. Res.*,
876 *81*(11), 1883-1902.

877 Lachenbruch, A. H., and G. A. Thompson (1972), Oceanic ridges and transform faults -
878 their intersection angles and resistance to plate motion, *Earth Planet Sci. Lett.*, *15*(2),
879 116-122.

880 Lizarralde, D., G. J. Axen, H. E. Brown, J. M. Fletcher, A. Gonzalez-Fernandez, A. J.
881 Harding, W. S. Holbrook, G. M. Kent, P. Paramo, F. Sutherland, and P. J. Umhoefer
882 (2007), Variation in styles of rifting in the Gulf of California, *Nature*, *448*(7152), 466-
883 469.

884 Macdonald, K. C., D. S. Scheirer, and S. M. Carbotte (1991), Mid-ocean ridges -
885 discontinuities, segments and giant cracks, *Science*, *253*(5023), 986-994.

886 Maurin, T., F. Masson, C. Rangin, U. T. Min, and P. Collard (2010), First global
887 positioning system results in northern Myanmar: Constant and localized slip rate along
888 the Sagaing fault, *Geology*, *38*(7), 591-594.

889 McCaffrey, R. (1992), Oblique plate convergence, slip vectors, and fore-arc deformation,
890 *J. Geophys. Res.*, *97*(B6), 8905-8915.

891 McCaffrey, R. (2009), The tectonic framework of the Sumatran subduction zone, *Annu.*
892 *Rev. Earth Planet. Sci.*, *37*, 345-366.

893 Menard, H. W., and T. Atwater (1968), Changes in direction of sea floor spreading,
894 *Nature*, 219(5153), 463-467.

895 Mukhopadhyay, B., and S. Dasgupta (2008), Swarms in Andaman Sea, India - a
896 seismotectonic analysis, *Acta Geophys.*, 56(4), 1000-1014.

897 Mutter, J. C., and J. A. Karson (1992), Structural processes at slow-spreading ridges,
898 *Science*, 257(5070), 627-634.

899 Pesicek, J. D., C. H. Thurber, H. Zhang, H. R. DeShon, E. R. Engdahl, and S.
900 Widiyantoro (2010), Teleseismic double-difference relocation of earthquakes along the
901 Sumatra-Andaman subduction zone using a 3-D model, *J. Geophys. Res.*, 115(B10303),
902 doi:10.1029/2010JB007443.

903 Poupinet, G., W. L. Ellsworth, and J. Frechet (1984), Monitoring velocity variations in
904 the crust using earthquake doublets - an application to the Calaveras Fault, California, *J.*
905 *Geophys. Res.*, 89(Nb7), 5719-5731.

906 Rangin, C., W. Maw, S. Lwin, W. Naing, C. Mouret, G. Bertrand, and GIAC scientific
907 party (1999), Cenozoic pull apart basins in central Burma; the trace of the path of India
908 along the western margin of Sundaland, paper presented at European Union of
909 Geosciences conferences, Strasbourg, France.

910 Rodolfo, K. S. (1969), Bathymetry and marine geology of Andaman Basin, and tectonic
911 implications for southeast Asia, *Geol. Soc. Amer. Bull.*, 80(7), 1203-1230.

912 Roland, E., and J.J. McGuire (2009), Earthquake swarms on transform faults, *Geophys. J.*
913 *Int.*, 178, 1677-1690.

914 Rubin, A. M. (1992), Dike-induced faulting and graben subsidence in volcanic rift zones,
915 *J. Geophys. Res.*, 97(B2), 1839-1858.

916 Schaff, D. P., G. H. R. Bokelmann, W. L. Ellsworth, E. Zankerka, F. Waldhauser, and G.
917 C. Beroza (2004), Optimizing correlation techniques for improved earthquake location,
918 *Bull. Seismol. Soc. Am.*, 94(2), 705-721.

919 Seeber, L., M. H. Cormier, C. McHugh, O. Emre, A. Polonia, and C. Sorlien (2006),
920 Rapid subsidence and sedimentation from oblique slip near a bend on the North
921 Anatolian transform fault in the Marmara Sea, Turkey, *Geology*, 34(11), 933-936.

922 Sempere, J. C., G. M. Purdy, and H. Schouten (1990), Segmentation of the Mid-Atlantic
923 Ridge between 24° N and 30° 40' N, *Nature*, 344(6265), 427-431.

924 Sevilgen, V., R. S. Stein, and F. F. Pollitz (2012), Stress imparted by the great 2004
925 Sumatra earthquake shut down transforms and activated rifts up to 400 km away in the
926 Andaman Sea, *P. Natl. Acad. Sci. USA*, 109(38), 15152-15156.

927 Shuler, A., M. Nettles, and G. Ekström (2013), Global observation of vertical-CLVD
928 earthquakes at active volcanoes, *J. Geophys. Res. Solid Earth*, 118,
929 doi:10.1029/2012JB009721.

930 Siebert, L., and T. Simkin (2002-). Volcanoes of the world: an illustrated catalog of
931 holocene volcanoes and their eruptions. *Smithsonian Institution, Global Volcanism*
932 *Program Digital Information Series, GVP-3*, (<http://www.volcano.si.edu/world/>).

933 Sieh, K., and D. Natawidjaja (2000), Neotectonics of the Sumatran fault, Indonesia, *J.*
934 *Geophys. Res.*, *105*, 28,295–228,326.

935 Singh, S. C., J. McArdle, K. Johansen, and K. A. K. Raju (2010), Seismic images of the
936 axial melt lens, Moho and deep penetrating faults at the sedimented Andaman Sea
937 Spreading Center, paper presented at Fall Meeting, AGU, San Francisco, Calif., 13-17
938 Dec.

939 Smith, W. H. F., and D. T. Sandwell (1997), Global sea floor topography from satellite
940 altimetry and ship depth soundings, *Science*, *277*(5334), 1956-1962.

941 Solomon, S. C., P. Y. Huang, and L. Meinke (1988), The seismic moment budget of
942 slowly spreading ridges, *Nature*, *334*(6177), 58-60.

943 Stein, R. S. (1999), The role of stress transfer in earthquake occurrence, *Nature*,
944 *402*(6762), 605-609.

945 Tanaka, A., and N. Fujii (1991), Energy-dissipation rates at ridge and transform-fault
946 segments - a model of oblique spreading, *Geophys. Res. Lett.*, *18*(5), 857-860.

947 Taylor, B., K. Crook, and J. Sinton (1994), Extensional transform zones and oblique
948 spreading centers, *J. Geophys. Res.*, *99*(B10), 19707-19718.

949 Thompson, G., and W. G. Melson (1972), Petrology of oceanic crust across fracture
950 zones in Atlantic Ocean - evidence of a new kind of sea-floor spreading, *J. Geol.*, 80(5),
951 526-538.

952 Tolstoy, M., D. R. Bohnenstiehl, M. H. Edwards, and G. J. Kurras (2001), Seismic
953 character of volcanic activity at the ultraslow-spreading Gakkel Ridge, *Geology*, 29(12),
954 1139-1142.

955 Tucholke, B. E., and J. Lin (1994), A geological model for the structure of ridge
956 segments in slow-spreading ocean crust, *J. Geophys. Res.*, 99(B6), 11937-11958.

957 Tuckwell, G. W., J. M. Bull, and D. J. Sanderson (1996), Models of fracture orientation
958 at oblique spreading centres, *J. Geol. Soc. London*, 153, 185-189.

959 Uyeda, S., and H. Kanamori (1979), Back-arc opening and the mode of subduction, *J.*
960 *Geophys. Res.*, 84(Nb3), 1049-1061.

961 Vigny, C., A. Socquet, C. Rangin, N. Chamotrooke, M. Pubellier, M. N. Bouin, G.
962 Bertrand, and M. Becker (2003), Present-day crustal deformation around Sagaing fault,
963 Myanmar, *J. Geophys. Res.*, 108(B11), doi: 10.1029/2002JB001999.

964 Waldhauser, F. (2009), Near-real-time double-difference event location using long-term
965 seismic archives, with application to Northern California, *Bull. Seismol. Soc. Am.*, 99(5),
966 2736-2748.

967 Waldhauser, F., and W. L. Ellsworth (2000), A double-difference earthquake location
968 algorithm: method and application to the northern Hayward fault, California, *Bull.*
969 *Seismol. Soc. Am.*, *90*(6), 1353-1368.

970 Waldhauser, F., and D. Schaff (2007), Regional and teleseismic double-difference
971 earthquake relocation using waveform cross-correlation and global bulletin data, *J.*
972 *Geophys. Res.*, *112*(B12), doi:10.1029/2007JB004938.

973 Waldhauser, F., D. P. Schaff, T. Diehl, and E. R. Engdahl (2012), Splay faults imaged by
974 fluid-driven aftershocks of the 2004 Mw 9.2 Sumatra-Andaman earthquake, *Geology*,
975 *40*(3), 243-246.

976 Walter, T.R., and F. Amelung (2007), Volcanic eruptions following $M \geq 9$ megathrust
977 earthquakes: implications for the Sumatra-Andaman volcanoes, *Geology*, *35*, 539-542,
978 doi: 10.1130/G23429A.1.

979 Wessel, P., and W. H. F. Smith (1998), New, improved version of the Generic Mapping
980 Tools released, *EOS, Trans. Am. geophys. Un.*, *79*, 579.

981

982 Widiyantoro, S., and R. van der Hilst (1997), Mantle structure beneath Indonesia inferred
983 from high-resolution tomographic imaging, *Geophys. J. Int.*, *130*(1), 167-182.

984

984 **Tables:**

Sector	Focal Mechanism	# CMTs	% of total M_0
WAF	All	18	23
	SS	6	4
	NF	8	16
	OS	4	3
ABSC	All	62	34
	NF	58	31
	OS	4	3
NE-BARC	All	34	37
	SS	10	15
	NF	8	4
	OS	16	18

985

986 **Table 1.** Distribution of seismic moment release M_0 from global CMT solutions in the Andaman Sea (Figure 4-6). The
 987 total seismic moment M_0 of all CMT solutions in the Andaman back-arc region (Figure 5) is $1.269 \cdot 10^{26}$ dyne-cm.
 988 Groups of focal mechanisms are defined in caption of Figure 4 (SS: strike-slip, NF: normal-fault, OS: oblique-slip).
 989 Gray boxes in Figure 6 define sectors of seismicity (NE-BARC sector is outlined by dashed line). Clusters C4 and C9
 990 outside of the three sectors (Figure 6) accommodate the remaining 6% of the total M_0 .

991

Start	On spreading segment	Duration of total activity (days)	Duration of main activity (days)*	# Events in ISC/EDR + DD-location	# Events with CMT + DD-location	Sum of CMT Moments [10^{26} dyne-cm]
1973/07/26 04:23	A	1	1	6	0	-
1984/07/05 20:46	C	40	7	80	12	0.117
1993/08/23 18:53	A+B	10	2	21	0	-
2006/03/09 14:45	B+C	23	3	137	24	0.168
2009/07/26 06:45	B+C	3	3	52	24	0.104
					Sum:	0.424

992

993 **Table 2.** Statistics of major earthquake swarms in the Andaman Back-Arc Spreading Center. Spreading segments are
 994 defined in Figure 7. *Duration of main activity is defined by consecutive days of ≥ 3 events per day.

995 **Figure Captions**

996

997 **Figure 1.** Simplified tectonic map of the Sumatra-Andaman region with active faults
998 indicated by solid and inactive faults marked as dashed black lines (after *Curray* [2005]).
999 Thin lines indicate the extensional horsetail system forming the southern termination of
1000 the Sagaing Fault as proposed by *Rangin et al.* [1999]. Dashed box indicates study area.
1001 Convergence rate is from *Sieh and Natawidjaja* [2000], spreading rate in the Andaman
1002 Sea is from *Kamesh Raju et al.* [2004]. Stars correspond to NEIC epicenters of the
1003 December 2004 Sumatra-Andaman and March 2005 Nias events. Corresponding global
1004 CMT solutions are plotted at their centroid locations. Triangles correspond to volcanic
1005 arc [*Siebert and Simkin*, 2002-]. Bold labels indicate plates. AB: Aceh Basin, ABSC:
1006 Andaman Back-Arc Spreading Center, AR: Alcock Rise, I-A: Indian-Australian, SEU:
1007 Seulimeum strand of the Sumatra Fault System, SFS: Sumatra Fault System, SR: Sewell
1008 Rise, WAF: West Andaman Fault.

1009

1010 **Figure 2.** Seismicity in the Sumatra-Andaman region as reported in the ISC and EDR
1011 bulletins for focal depths ≤ 40 km. (a) Time period: January 1 1964 to December 25 2004.
1012 Blue dots correspond to events between 1983-1984; green dots indicate events between
1013 1993-1994. Stars indicate epicenters of the 2004 Sumatra-Andaman earthquake and 2005
1014 Nias earthquake. Dashed line indicates outline of back-arc region studied. (b) Time
1015 period: December 26 2004 ($M_w=9.2$ Sumatra-Andaman earthquake) to March 28 2005.
1016 Yellow line indicates rupture area of the 2004 Sumatra-Andaman earthquake based on
1017 the slip model of *Chlieh et al.* [2007]. (c) Time period: 2005/03/28 ($M_w=8.7$ Nias

1018 earthquake) to end of 2009. Yellow dots correspond to events in 2006; red dots indicate
1019 events in 2009. Brown line indicates rupture area of the 2005 Nias earthquake based on
1020 the slip model of *Briggs et al.* [2006].

1021

1022 **Figure 3.** Percentage of correlated events within volumes of 50 x 50 x 50 km between 0
1023 and 50 km depth. Correlated events in the map are defined to have at least four
1024 correlation measurements with cross-correlation coefficients ≥ 0.8 over less than 50 km
1025 hypocenter separation. Volumes with less than 5 events and events with less than 4
1026 waveforms are not included. Crosses indicate volumes with more than 5 events but with
1027 no waveform data available. Epicenters of Mw=9.2 and Mw=8.7 earthquakes are
1028 indicated by stars. Green lines indicate tectonic features (after *Curray* [2005]). Triangles
1029 denote to volcanic arc [*Siebert and Simkin*, 2002-]. Blue boxes include cluster C1 and C3
1030 shown in Figure 4. AB: Aceh Basin, ABSC: Andaman Back-Arc Spreading Center, AR:
1031 Alcock Rise.

1032

1033 **Figure 4.** (a)-(b) Comparison of ISC/EDR bulletin locations (top row) with DD-results
1034 (bottom row) for seismicity clusters C1 (see blue box in Figure 3 for location). Blue dots:
1035 Jul. 2003; red: Jul. to Aug. 2004. Bold pink line indicates strike of normal fault inferred
1036 from cluster orientation and CMT solutions. Bold blue line indicates strike of adjacent
1037 transform fault inferred from CMT solutions and bathymetry. (c)-(d) Comparison of
1038 ISC/EDR bulletin locations (top row) with DD-results (bottom row) for seismicity
1039 clusters C3 (see blue box in Figure 3 for location). Orange dots: Dec. 1983; yellow: Jan.
1040 1984; blue: Jan. 2003. Stars indicate initiation of sequences. The red line marks the width

1041 of the rift valley identified by *Curray* [2005] along the NW-SE oriented seismic
1042 reflection profile I19-29. Contour lines correspond to satellite bathymetry between -2900
1043 and -2600 m; gray dash-dotted line indicates notional plate boundary. Global CMT
1044 solutions in Figure 4b and 4d are color-coded by type of faulting: red=normal-fault
1045 (plunge of P-axis $\geq 60^\circ$, plunge of B- and T-axis $\leq 45^\circ$); blue=strike-slip (plunge of B-axis
1046 $\geq 60^\circ$, plunge of P- and T-axis $\leq 45^\circ$); gray=oblique-slip (mechanisms, which fall outside
1047 normal-fault and strike-slip definitions). Black lines on the beach-ball symbols indicate
1048 nodal planes of the double-couple part of the moment tensor. Bars correspond to
1049 orientation of T-axes from CMT solutions. Label left of beach-ball symbols denotes
1050 year/month of event. Gray ellipses indicate the 90% confidence interval of relative
1051 locations derived from bootstrap analysis.

1052

1053 **Figure 5.** Map with DD locations (black dots) and associated global CMT solutions for
1054 the Andaman Back-Arc region. CMT solutions are color-coded and annotated as in
1055 Figure 4. Solutions labeled O1-O4 and S3-S5 in the NE part are discussed in text,
1056 numbers in brackets next to the labels denote focal depths as reported in the EHB catalog.
1057 Solutions labeled vPC1-vPC1 indicate potential vertical-CLVD mechanisms. Background
1058 satellite bathymetry is sampled on a grid of 30 arc-seconds [*GEBCO_08 Grid*,
1059 <http://www.gebco.net>] with a horizontal resolution in the order of several kilometers in
1060 the Andaman Sea [*Smith and Sandwell, 1997*]. Bathymetry in the vicinity of the ABSC
1061 has a horizontal resolution of 200 m [*Kamesh Raju et al., 2004*]. Thin lines indicate the
1062 extensional horsetail system forming the southern termination of the Sagaing Fault as
1063 proposed by *Rangin et al.* [1999]. AR: Alcock Rise.

1064

1065 **Figure 6.** Plate boundaries and associated slip directions in the Andaman Sea based on
1066 DD relocations (black dots; focal depths ≤ 50 km.), CMT solutions, and bathymetry data.
1067 Faults west of the spreading center are from *Curray* [2005]. Spreading segments are from
1068 *Kamesh Raju et al.* [2004]. Thin lines indicate the extensional horsetail system forming
1069 the southern termination of the Sagaing Fault as proposed by *Rangin et al.* [1999].
1070 Direction of CMT T-axes of normal-faulting events (where P-axes plunge $\geq 60^\circ$) indicates
1071 direction of maximum extensional strain and is represented by white arrows. Black bars
1072 indicate strike of dextral nodal planes of the strike-slip events (where B-axes plunge
1073 $\geq 60^\circ$). Areas outlined by gray lines define different sectors of the Andaman Sea as
1074 discussed in the text. AR: Alcock Rise; BI: Barren Island.

1075

1076 **Figure 7.** (a) Map with DD locations (dots) in the Andaman Back-Arc Spreading Center
1077 (see black box in Figure 5). Gray: background seismicity; magenta: seismicity in 1973;
1078 blue: seismicity in 1984; green: 1993; yellow: 2006; red: 2009. Gray ellipses indicate
1079 90% confidence interval for relative locations derived from bootstrap analysis. Bars
1080 correspond to surface projections of B-axes of global CMT solutions of normal faulting
1081 events; gray arrows correspond to surface projections of the CMT slip-vector (preferred
1082 fault plane); Beach-ball symbols indicate composite moment tensors of individual
1083 swarms and all CMT solutions. High-resolution bathymetry (grid of 100 m) is from
1084 *Kamesh Raju et al.* [2004]. Ridge segments A-C [*Kamesh Raju et al.*, 2004] are indicated
1085 by brown lines. D-D' shows location of depth profile in Figure 7b for events included in
1086 box. (b) Depth cross-section along profile D-D'. Circles and dots are hypocenters using

1087 the same color scheme as in Figure 7a. Error bars indicate the 90% confidence interval of
1088 relative depth derived from bootstrap analysis. Global CMT solutions are shown as
1089 projections to the depth profile. Note vertical exaggeration of bathymetry cross-section.
1090 FS: Fault Scarp; NVZ: Neovolcanic Zone.

1091

1092 **Figure 8.** (a) Location of along-ridge profile and DD-epicenters in the Andaman
1093 Spreading Center. Solid white line indicates along-strike extent of a hypothetical dike
1094 opening used for Coulomb stress change modeling. Dashed white lines (F, G) indicate
1095 location of Coulomb stress change profiles discussed in text. (b)-(c) Origin time versus
1096 distance along ridge axis for three major swarms in the Andaman Spreading Center.
1097 Position of first event of each swarm is indicated by vertical dashed gray line. Black lines
1098 indicate possible propagation velocities. Focal mechanisms in (b) indicate location and
1099 timing of oblique mechanism O5 and vertical-P CLVD mechanism vPC1 during the 1984
1100 swarm.

1101

1102 **Figure 9.** Left: Bathymetry profiles across the ABSC derived from the high-resolution
1103 grid of *Kamesh Raju et al.* [2004]. Tracks and origins of selected profiles are shown in
1104 Figure 10a. Numbers on the left indicate index of profile. Spacing between profiles is 2.5
1105 km. Crosses mark position of maximum axial depression on each profile. Gray dashed
1106 lines indicate possible fault scarps; black dotted lines suggest notional geometry of
1107 normal faults. Right: Depth of maximum axial depression of each profile. Black arrows
1108 indicate position of ridge discontinuities (TD: Transform Discontinuity; NTD: Non-
1109 Transform Discontinuity).

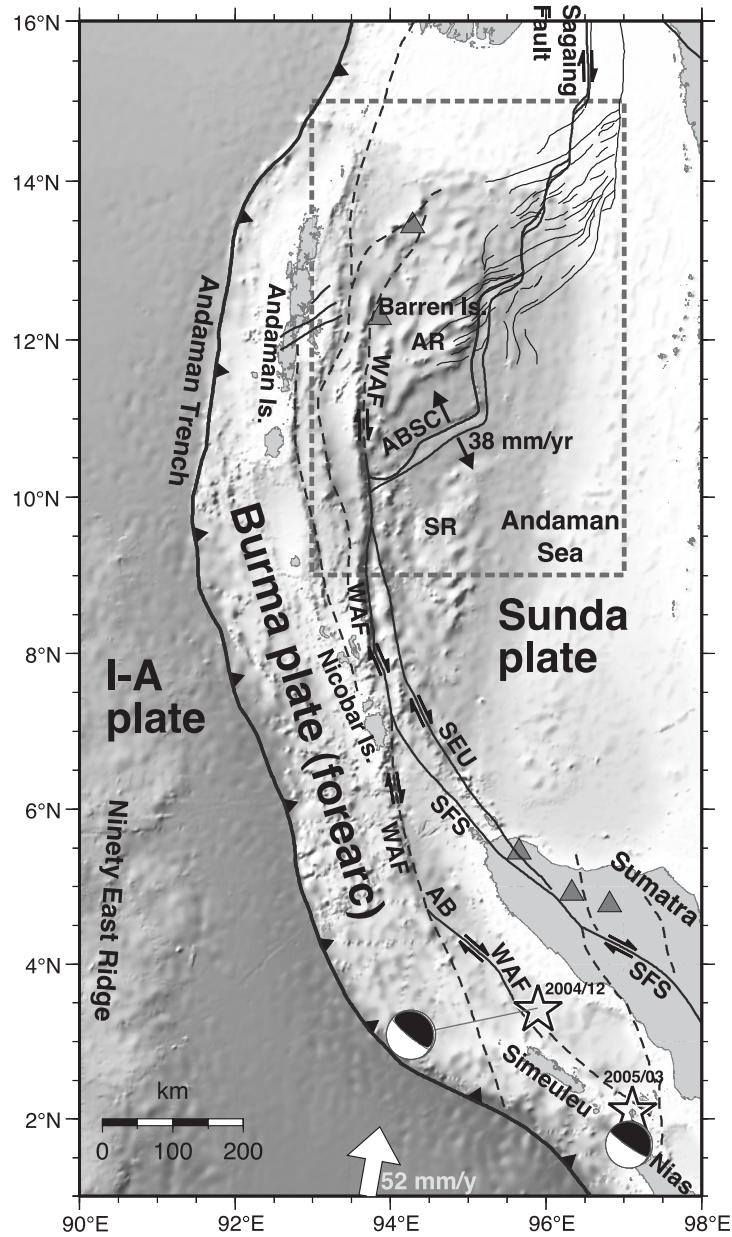
1110

1111 **Figure 10.** (a) Location of along-ridge profile, DD epicenters, preferred fault planes, and
1112 tracks of bathymetry profiles shown in Figure 9. (b)-(d) Dip, strike, and rake of preferred
1113 fault planes along the ridge axis. CMT solutions for which a preferred fault plane has
1114 been determined are indicated by black bold dots and squares (dots: preferred fault plane
1115 dipping to SE; squares: preferred fault plane dipping to NW). White square indicates
1116 vertical-P CLVD mechanisms vPC1. For CMT solutions without preferred plane (gray
1117 dots) azimuths of B-axes are shown in Figure 10c. Dashed-dotted line in Figure 10c
1118 indicates direction of maximum extensional strain plus 90° as derived from composite
1119 CMT solutions along segment C. Rose diagram in Figure 10c shows orientation of fault
1120 strike or B-axis of CMT solutions along segment C.

1121

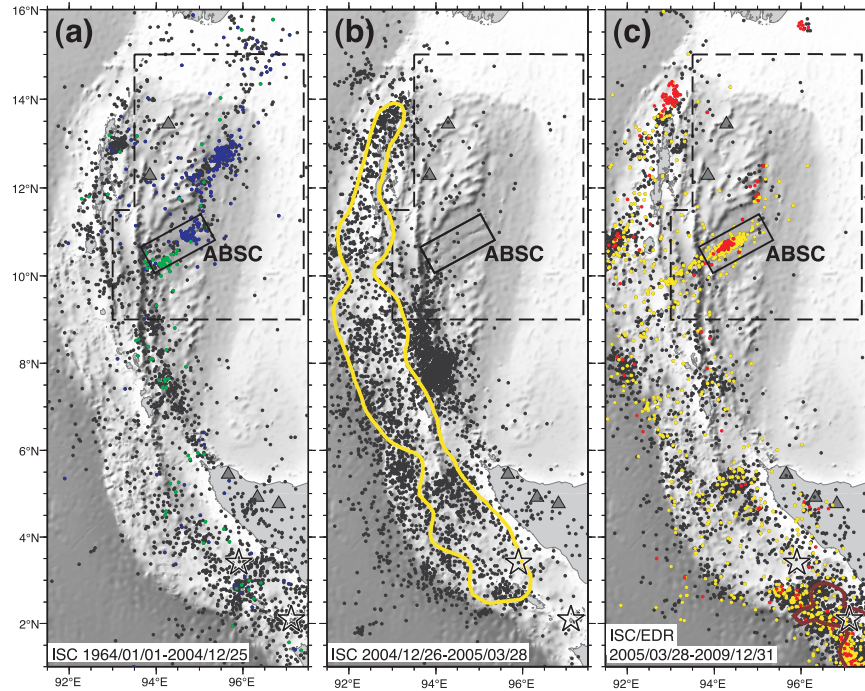
1122 **Figure 11.** (a) Conceptual end-member models of non-orthogonal ridge-transform
1123 geometry. *SD*: long-term spreading direction [Curry, 2005]. Trend of ridge and
1124 transform faults are based on the ABSC geometry. (b) Summary of the ridge geometry of
1125 the ABSC. *TC*: direction of composite tension axis of CMT solutions at segment C; *SC*:
1126 median strike of nodal planes at segment C (inset Figure 10c).

1127



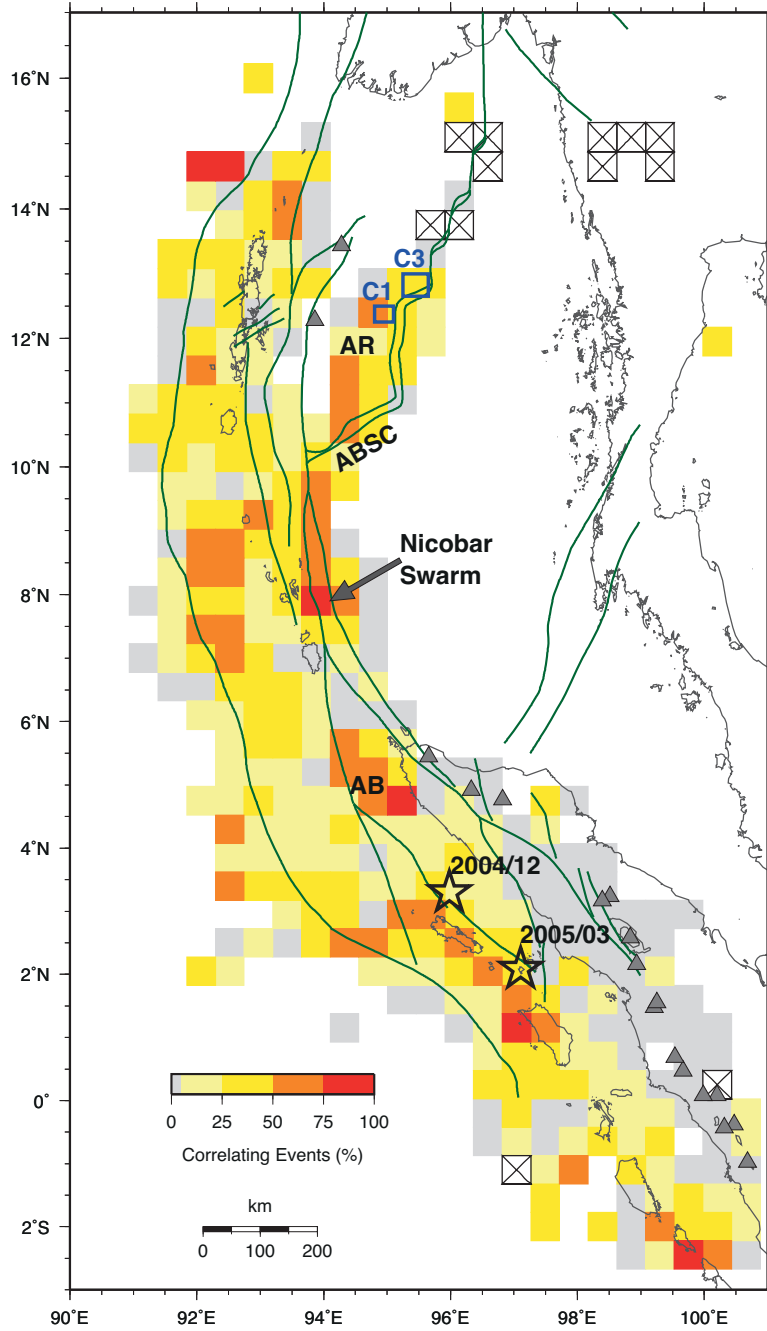
1128

1129 **Figure 1.** Simplified tectonic map of the Sumatra-Andaman region with active faults indicated by solid and inactive faults marked as
 1130 dashed lines (after *Curry* [2005]). Thin lines indicate the extensional horsetail system forming the southern termination of the
 1131 Sagaing Fault as proposed by *Rangin et al.* [1999]. Dashed box indicates study area. Convergence rate is from *Sieh and Natawidjaja*
 1132 [2000], spreading rate in the Andaman Sea is from *Kamesh Raju et al.* [2004]. Stars correspond to NEIC epicenters of the December
 1133 2004 Sumatra-Andaman and March 2005 Nias events. Corresponding global CMT solutions are plotted at their centroid locations.
 1134 Triangles correspond to volcanic arc [*Siebert and Simkin, 2002-*]. Bold labels indicate plates. AB: Aceh Basin, ABSC: Andaman
 1135 Back-Arc Spreading Center, AR: Alcock Rise, I-A: Indian-Australian, SEU: Seulimeum strand of the Sumatra Fault System, SFS:
 1136 Sumatra Fault System, SR: Sewell Rise, WAF: West Andaman Fault.



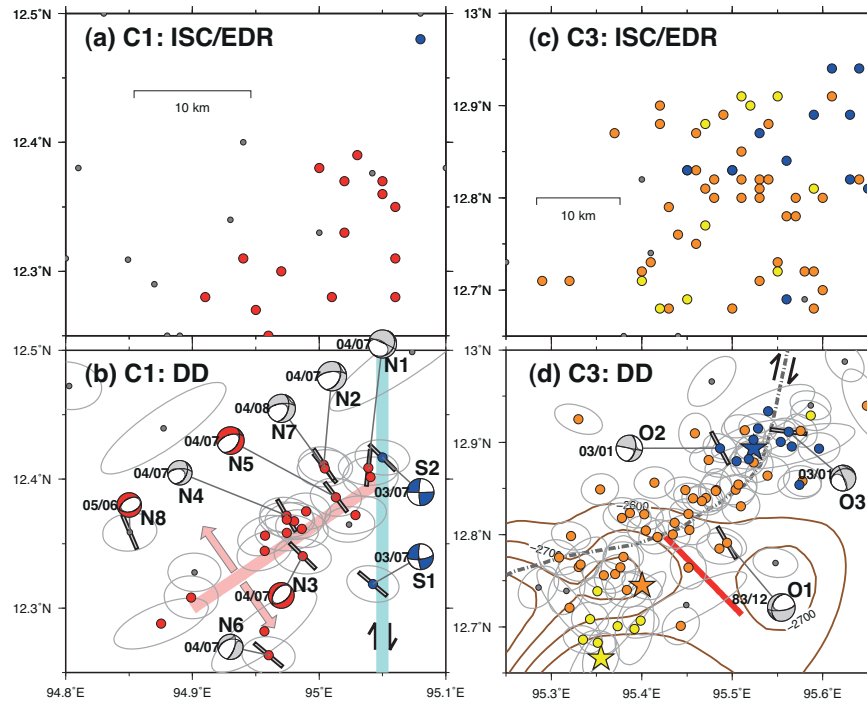
1137

1138 **Figure 2.** Seismicity in the Sumatra-Andaman region as reported in the ISC and EDR bulletins for focal depths ≤ 40 km. (a) Time
 1139 period: January 1 1964 to December 25 2004. Blue dots correspond to events between 1983-1984; green dots indicate events between
 1140 1993-1994. Stars indicate epicenters of the 2004 Sumatra-Andaman earthquake and 2005 Nias earthquake. Dashed line indicates
 1141 outline of back-arc region studied. (b) Time period: December 26 2004 ($M_w=9.2$ Sumatra-Andaman earthquake) to March 28 2005.
 1142 Yellow line indicates rupture area of the 2004 Sumatra-Andaman earthquake based on the slip model of *Chlieh et al.* [2007]. (c) Time
 1143 period: 2005/03/28 ($M_w=8.7$ Nias earthquake) to end of 2009. Yellow dots correspond to events in 2006; red dots indicate events in
 1144 2009. Brown line indicates rupture area of the 2005 Nias earthquake based on the slip model of *Briggs et al.* [2006].



1145

1146 **Figure 3.** Percentage of correlated events within volumes of 50 x 50 km between 0 and 50 km depth. Correlated events in the
 1147 map are defined to have at least four correlation measurements with cross-correlation coefficients ≥ 0.8 over less than 50 km
 1148 hypocenter separation. Volumes with less than 5 events and events with less than 4 waveforms are not included. Crosses indicate
 1149 volumes with more than 5 events but with no waveform data available. Epicenters of Mw=9.2 and Mw=8.7 earthquakes are indicated
 1150 by stars. Green lines indicate tectonic features (after *Curray [2005]*). Triangles denote to volcanic arc [*Siebert and Simkin, 2002-*].
 1151 Blue boxes include cluster C1 and C3 shown in Figure 4. AB: Aceh Basin, ABSC: Andaman Back-Arc Spreading Center, AR: Alcock
 1152 Rise.



1153

1154

1155

1156

1157

1158

1159

1160

1161

1162

1163

1164

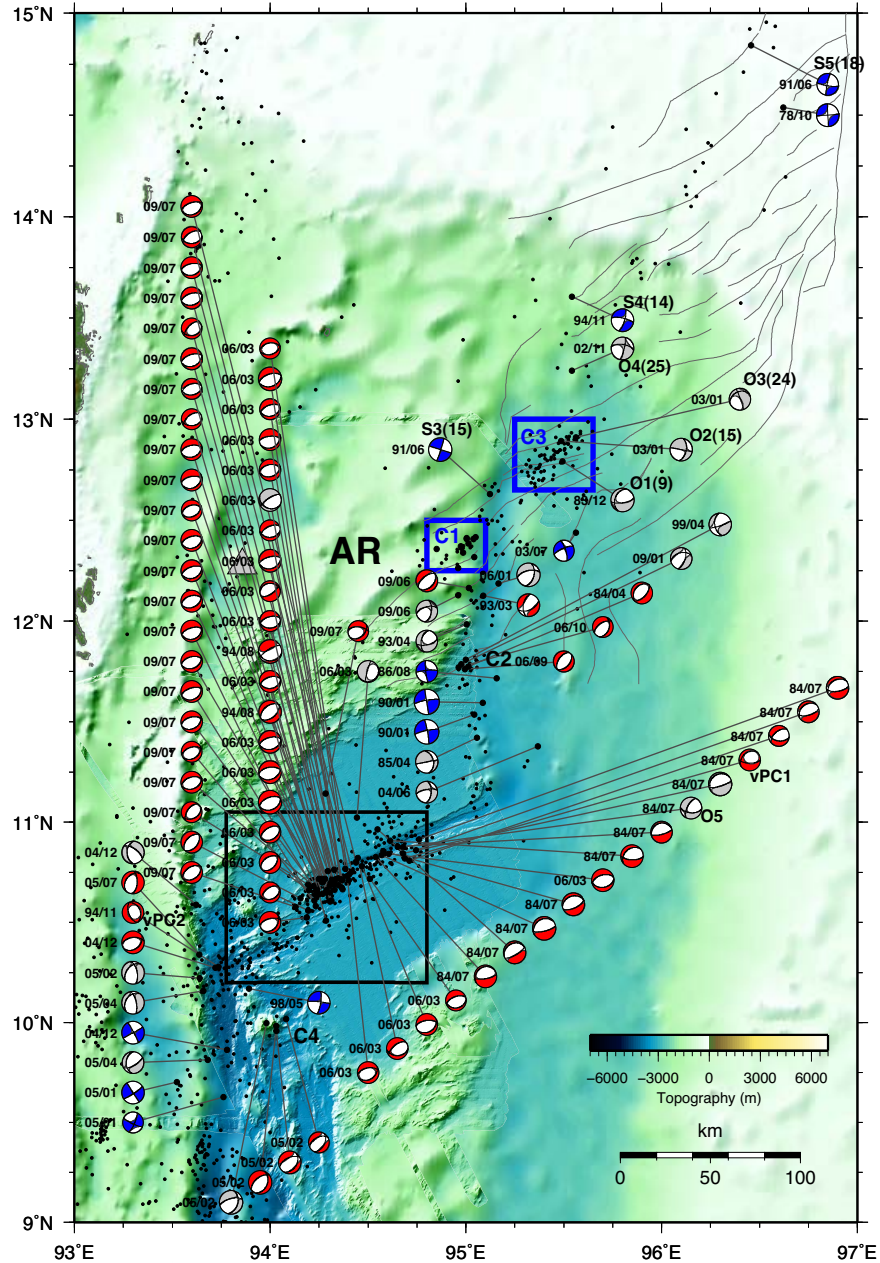
1165

1166

1167

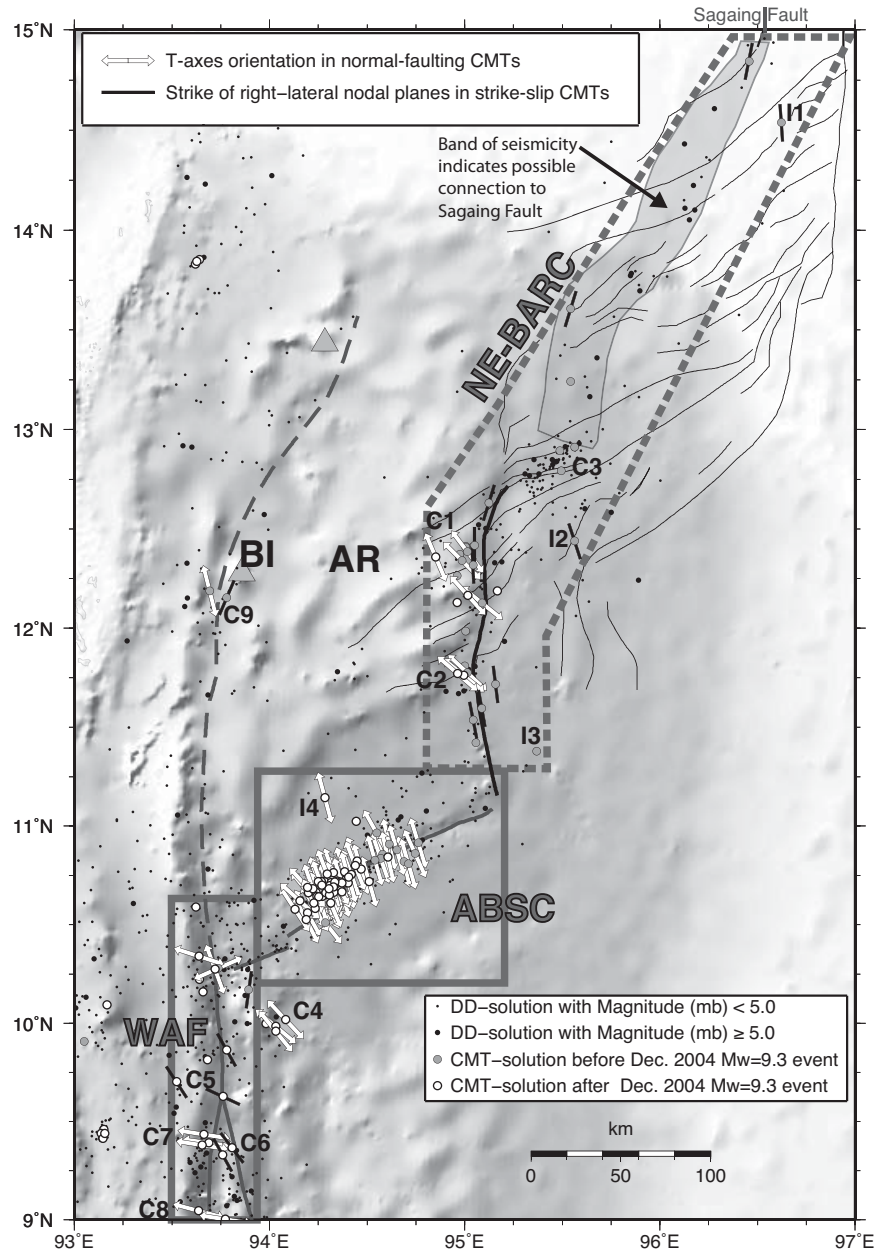
1168

Figure 4. (a)-(b) Comparison of ISC/EDR bulletin locations (top row) with DD-results (bottom row) for seismicity clusters C1 (see blue box in Figure 3 for location). Blue dots: Jul. 2003; red: Jul. to Aug. 2004. Bold pink line indicates strike of normal fault inferred from cluster orientation and CMT solutions. Bold blue line indicates strike of adjacent transform fault inferred from CMT solutions and bathymetry. (c)-(d) Comparison of ISC/EDR bulletin locations (top row) with DD-results (bottom row) for seismicity clusters C3 (see blue box in Figure 3 for location). Orange dots: Dec. 1983; yellow: Jan. 1984; blue: Jan. 2003. Stars indicate initiation of sequences. The red line marks the width of the rift valley identified by Curray [2005] along the NW-SE oriented seismic reflection profile I19-29. Contour lines correspond to satellite bathymetry between -2900 and -2600 m; gray dash-dotted line indicates notional plate boundary. Global CMT solutions in Figure 4b and 4d are color-coded by type of faulting: red=normal-fault (plunge of P-axis $\geq 60^\circ$, plunge of B- and T-axis $\leq 45^\circ$); blue=strike-slip (plunge of B-axis $\geq 60^\circ$, plunge of P- and T-axis $\leq 45^\circ$); gray=oblique-slip (mechanisms, which fall outside normal-fault and strike-slip definitions). Black lines on the beach-ball symbols indicate nodal planes of the double-couple part of the moment tensor. Bars correspond to orientation of T-axes from CMT solutions. Label left of beach-ball symbols denotes year/month of event. Gray ellipses indicate the 90% confidence interval of relative locations derived from bootstrap analysis.



1169

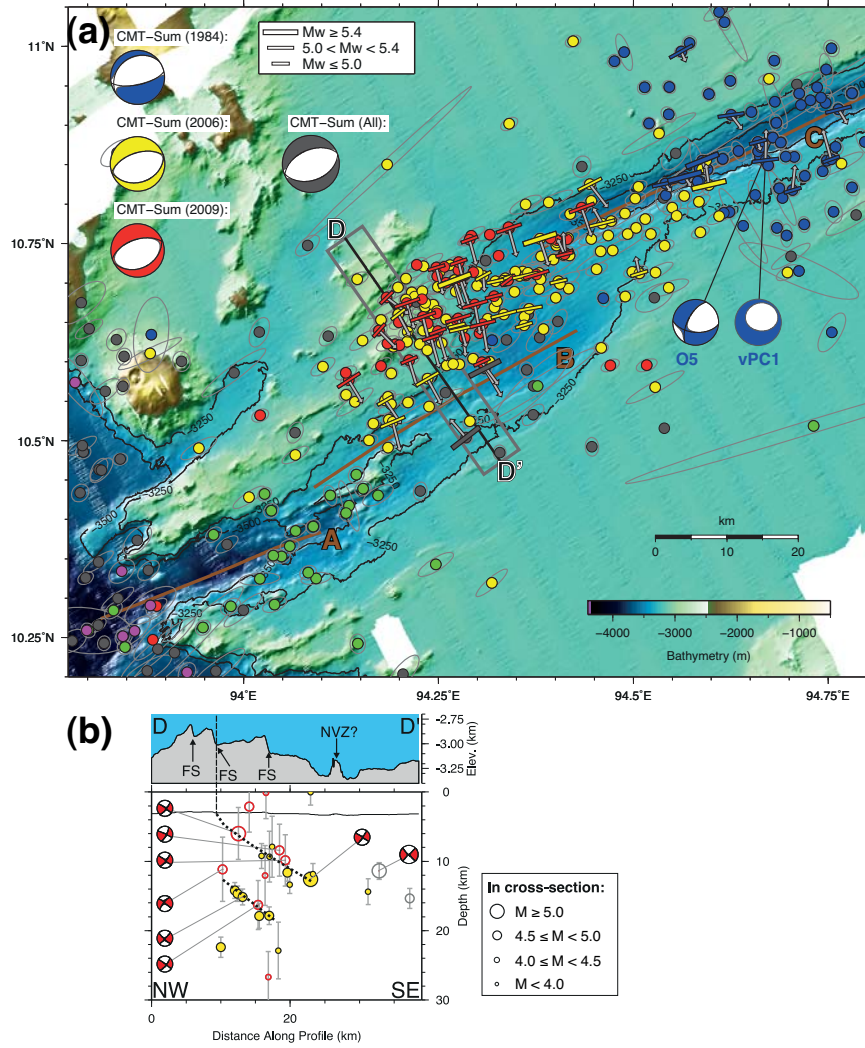
1170 **Figure 5.** Map with DD locations (black dots) and associated global CMT solutions for the Andaman Back-Arc region. CMT
 1171 solutions are color-coded and annotated as in Figure 4. Solutions labeled O1-O4 and S3-S5 in the NE part are discussed in text,
 1172 numbers in brackets next to the labels denote focal depths as reported in the EHB catalog. Solutions labeled vPC1-vPC1 indicate
 1173 potential vertical-CLVD mechanisms. Background satellite bathymetry is sampled on a grid of 30 arc-seconds [*GEBCO_08 Grid*,
 1174 *http://www.gebco.net*] with a horizontal resolution in the order of several kilometers in the Andaman Sea [*Smith and Sandwell, 1997*].
 1175 Bathymetry in the vicinity of the ABSC has a horizontal resolution of 200 m [*Kamesh Raju et al., 2004*]. Thin lines indicate the
 1176 extensional horsetail system forming the southern termination of the Sagaing Fault as proposed by Rangin et al. [1999]. AR: Alcock
 1177 Rise.



1178

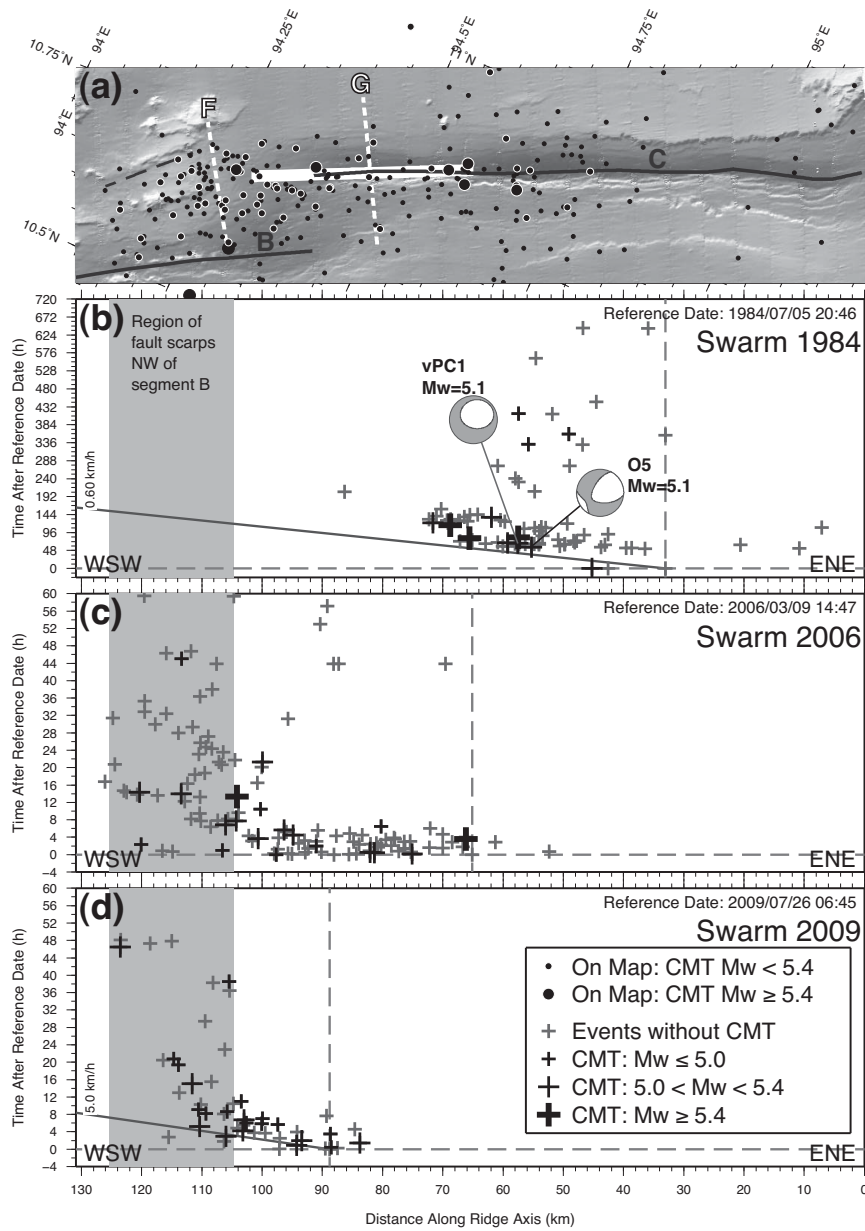
1179 **Figure 6.** Plate boundaries and associated slip directions in the Andaman Sea based on DD relocations (black dots; focal depths ≤ 50
 1180 km.), CMT solutions, and bathymetry data. Faults west of the spreading center are from *Curray* [2005]. Spreading segments are from
 1181 *Kamesh Raju et al.* [2004]. Thin lines indicate the extensional horsetail system forming the southern termination of the Sagaing Fault
 1182 as proposed by *Rangin et al.* [1999]. Direction of CMT T-axes of normal-faulting events (where P-axes plunge $\geq 60^\circ$) indicates
 1183 direction of maximum extensional strain and is represented by white arrows. Black bars indicate strike of dextral nodal planes of the
 1184 strike-slip events (where B-axes plunge $\geq 60^\circ$). Areas outlined by bold gray lines define different sectors of the Andaman Sea as
 1185 discussed in the text. AR: Alcock Rise; BI: Barren Island.

1186



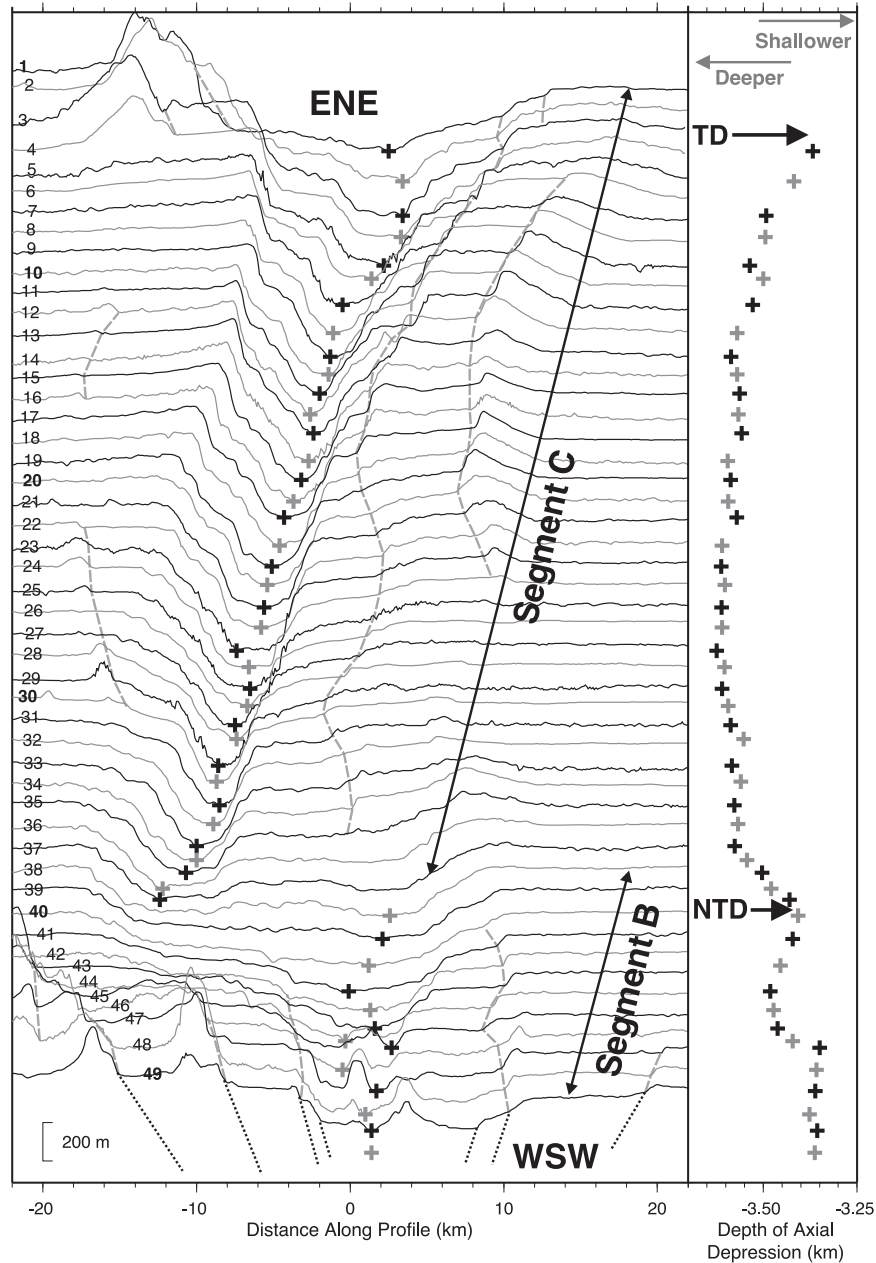
1187

1188 **Figure 7.** (a) Map with DD locations (dots) in the Andaman Back-Arc Spreading Center (see black box in Figure 5). Gray:
 1189 background seismicity; magenta: seismicity in 1973; blue: seismicity in 1984; green: 1993; yellow: 2006; red: 2009. Gray ellipses
 1190 indicate 90% confidence interval for relative locations derived from bootstrap analysis. Bars correspond to surface projection of B-
 1191 axes of global CMT solutions of normal faulting events; gray arrows correspond to surface projections of the CMT slip-vector
 1192 (preferred fault plane); Beach-ball symbols indicate composite moment tensors of individual swarms and all CMT solutions. High-
 1193 resolution bathymetry (grid of 100 m) is from *Kamesh Raju et al.* [2004]. Ridge segments A-C [*Kamesh Raju et al.*, 2004] are
 1194 indicated by brown lines. D-D' shows location of depth profile in Figure 7b for events included in box. (b) Depth cross-section along
 1195 profile D-D'. Circles and dots are hypocenters using the same color scheme as in Figure 7a. Error bars indicate the 90% confidence
 1196 interval of relative depth derived from bootstrap analysis. Global CMT solutions are shown as projections to the depth profile. Note
 1197 vertical exaggeration of bathymetry cross-section. FS: Fault Scarp; NVZ: Neovolcanic Zone.



1198

1199 **Figure 8.** (a) Location of along-ridge profile and DD-epicenters in the Andaman Spreading Center. Solid white line indicates along-
 1200 strike extent of a hypothetical dike opening used for Coulomb stress change modeling. Dashed white lines (F, G) indicate location of
 1201 Coulomb stress change profiles discussed in text. (b)-(c) Origin time versus distance along ridge axis for three major swarms in the
 1202 Andaman Spreading Center. Position of first event of each swarm is indicated by vertical dashed gray line. Solid lines in (b) and (d)
 1203 indicate possible propagation velocities. Focal mechanisms in (b) indicate location and timing of oblique mechanism O5 and vertical-
 1204 P CLVD mechanism vPC1 during the 1984 swarm.



1205

1206

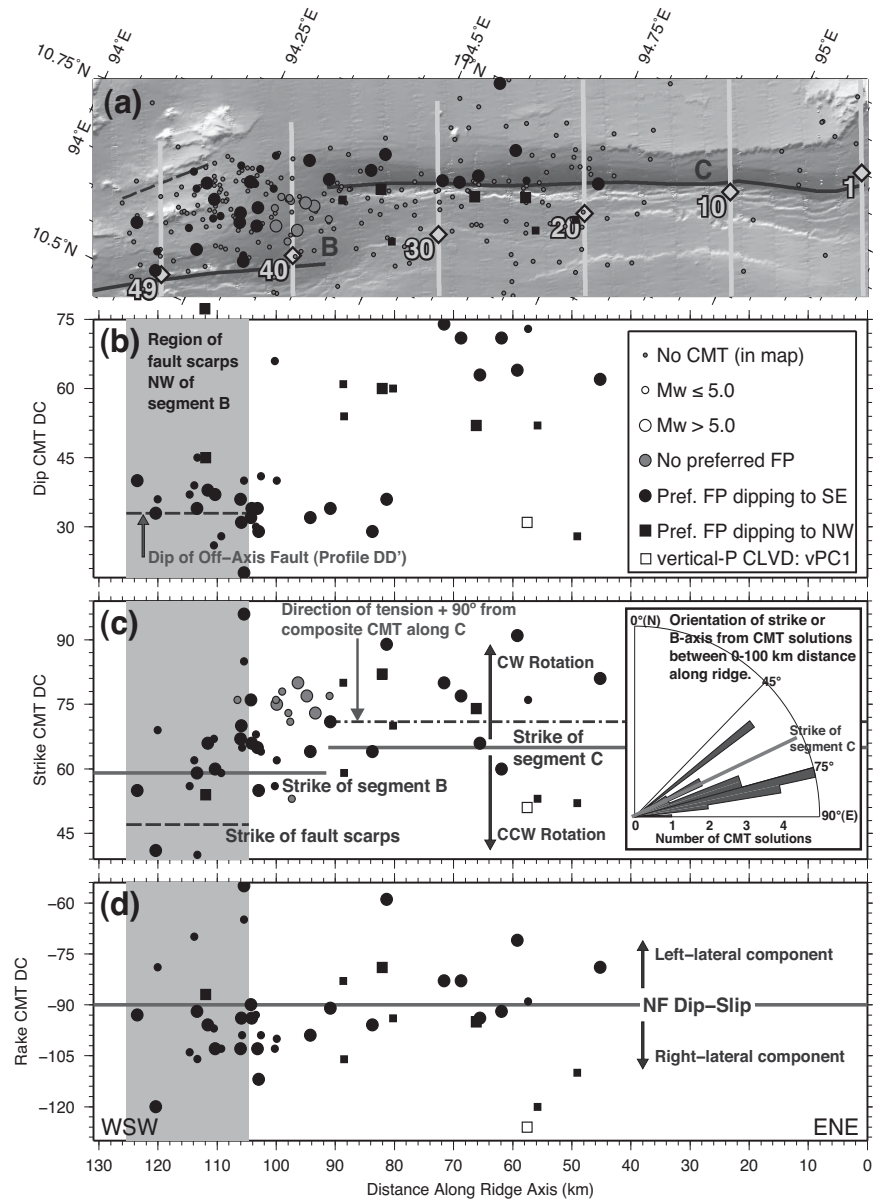
1207

1208

1209

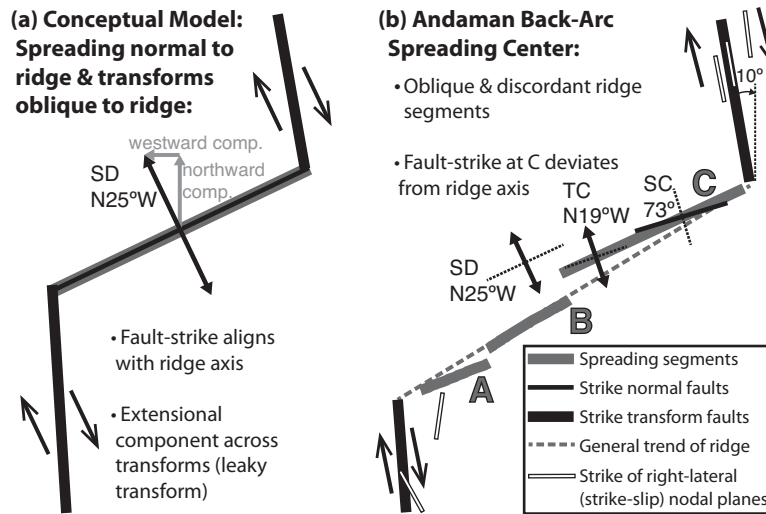
1210

Figure 9. Left: Bathymetry profiles across the ABCS derived from the high-resolution grid of *Kamesh Raju et al.* [2004]. Tracks and origins of selected profiles are shown in Figure 10a. Numbers on the left indicate index of profile. Spacing between profiles is 2.5 km. Crosses mark position of maximum axial depression on each profile. Gray dashed lines indicate possible fault scarps; black dotted lines suggest notional geometry of normal faults. Right: Depth of maximum axial depression of each profile. Black arrows indicate position of ridge discontinuities (TD: Transform Discontinuity; NTD: Non-Transform Discontinuity).



1211

1212 **Figure 10.** (a) Location of along-ridge profile, DD epicenters, preferred fault planes, and tracks of bathymetry profiles shown in
 1213 Figure 9. (b)-(d) Dip, strike, and rake of preferred fault planes along the ridge axis. CMT solutions for which a preferred fault plane
 1214 has been determined are indicated by black bold dots and squares (dots: preferred fault plane dipping to SE; squares: preferred fault
 1215 plane dipping to NW). White square indicates vertical-P CLVD mechanisms vPC1. For CMT solutions without preferred plane (gray
 1216 dots) azimuths of B-axes are shown in Figure 10c. Dashed-dotted line in Figure 10c indicates direction of maximum extensional strain
 1217 plus 90° as derived from composite CMT solutions along segment C. Rose diagram in Figure 10c shows orientation of fault strike or
 1218 B-axis of CMT solutions along segment C.



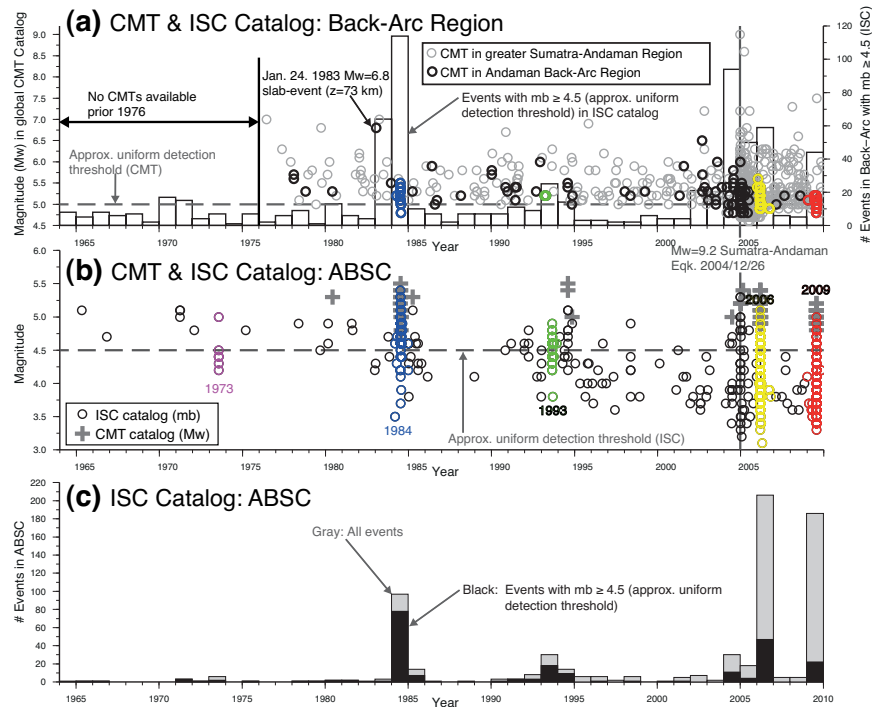
1219

1220 **Figure 11.** (a) Conceptual end-member models of non-orthogonal ridge-transform geometry. SD: long-term spreading direction
 1221 [Curry, 2005]. Trend of ridge and transform faults are based on the ABSC geometry. (b) Summary of the ridge geometry of the
 1222 ABSC. TC: direction of composite tension axis of CMT solutions at segment C; SC: median strike of nodal planes at segment C (inset
 1223 Figure 10c).
 1224

1224 **Electronic Supplement**

1225 **S.1 Characteristics of earthquake sequences in the Andaman Sea**

1226 Figure S1 describes the overall temporal clustering of seismicity in the back-arc region
1227 between 1964 and 2009. Figures S2-S4 illustrate the characteristics of different
1228 earthquake sequences in the back-arc region in terms of event time and magnitude.
1229

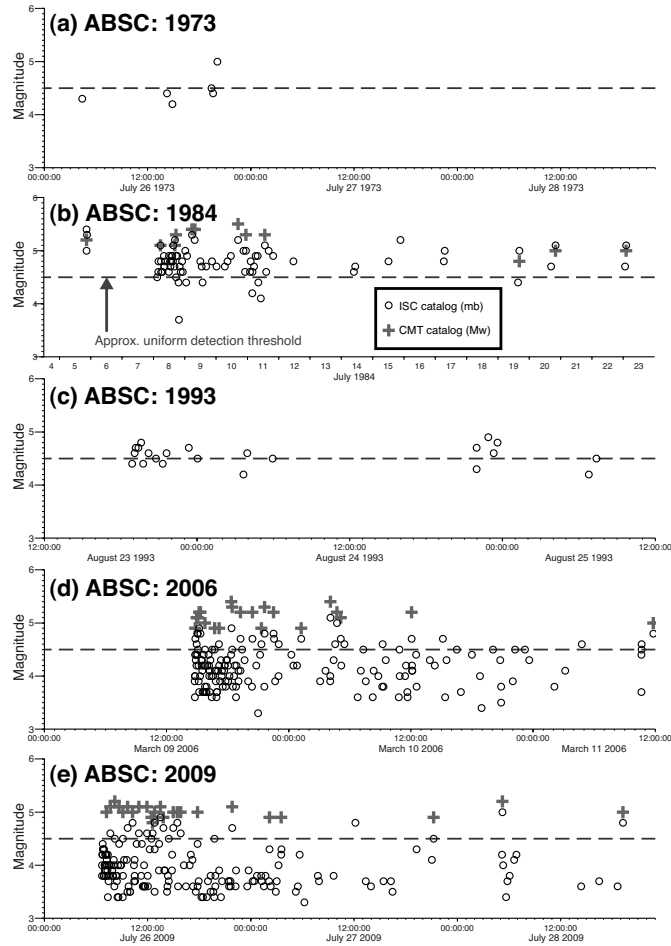


1230

1231 **Figure S1.** Seismicity in the Andaman Sea back-arc region between 1964 and 2009. (a) Thin gray circles indicate Mw in the greater
1232 Sumatra-Andaman region (area shown in Figure 1) as reported in the global CMT catalog. Bold circles indicate Mw in the back-arc
1233 region as reported in the global CMT catalog. Histogram in the background indicates number of events per year (with $m_b \geq 4.5$) in the
1234 back-arc region as reported in the ISC catalog. (b) Circles indicate m_b for earthquakes within the Andaman Back-Arc Spreading
1235 Center (ABSC) as reported in the ISC catalog. Crosses indicate Mw for earthquakes within the ABSC as reported in the global CMT
1236 catalog. (c) Number of events per year in the ABSC as reported in the ISC catalog. Gray indicates all events in the ABSC. To account
1237 for a uniform detection threshold, black bars indicates number of events with $m_b \geq 4.5$.

1238

1239



1240

1241

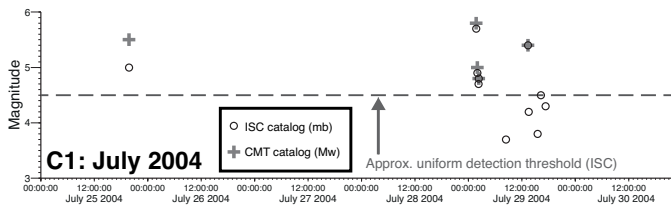
1242

1243

1244

1245

Figure S2. Characteristics of earthquake sequences in the ABSC in terms of event time and magnitude. Circles indicate mb as reported in the ISC catalog. Crosses indicate Mw as reported in the global CMT catalog. Typical for swarm-like sequences, the largest magnitudes occur in the middle of the sequences and magnitudes do not decay as observed in typical mainshock-aftershock sequences.



1246

1247

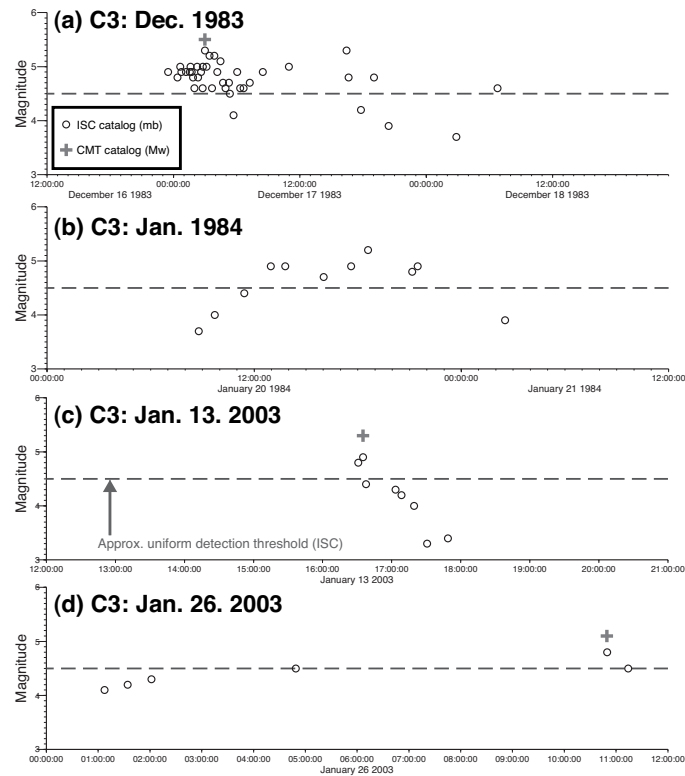
1248

1249

1250

1251

Figure S3. Characteristics of an earthquake sequence in the northeastern part of the back-arc region (cluster C1 in Figure 4b and 5) in terms of event time and magnitude. Circles indicate mb as reported in the ISC catalog. Crosses indicate Mw as reported in the global CMT catalog. A precursor-event on July 25 is followed by the main-shock on July 29, 2004. In contrast to the swarms in the ABSC, magnitudes rapidly decrease after the mainshock, suggesting a typical mainshock-aftershock behavior of this sequence.



1252

1253 **Figure S4.** Characteristics of earthquake sequences in the northeastern part of the back-arc region (cluster C3 in Figure 4d and 5) in
 1254 terms of event time and magnitude. Circles indicate mb as reported in the ISC catalog. Crosses indicate Mw as reported in the global
 1255 CMT catalog. Sequences in a, b, d show typical swarm-like characteristics, whereas the sequence in c indicates a mainshock-
 1256 aftershock behavior.

1257

1258 **S.2 Assessment of absolute location robustness**

1259 Accuracy in absolute locations is crucial for interpretation of underlying mechanisms,
 1260 especially if seismicity is correlated with surface structures (e.g. seafloor morphology).

1261 The absolute position of DD-solutions strongly depends on the accuracy of the initial
 1262 hypocenters. Since the EHB locations are the reference base for the overall absolute

1263 location of the DD solutions, possible bias in the EHB locations would also affect the
 1264 absolute position of the DD-solutions. Such bias may result from deviations of the true

1265 structure from the 1D velocity model ak135 used to locate the events (presence of slab,
 1266 etc.) and bias in station geometry.

1267

1268 To assess the effect of source-side 3D velocity structure on the location of earthquakes in
1269 the Andaman Sea, we calculated theoretical *P*-wave travel times (first arriving phases
1270 only; distances $\leq 95^\circ$) in a 3D velocity model [*Widiyantoro and van der Hilst, 1997*] for a
1271 series of synthetic hypocenters (black dots in Figure S5). A synthetic, symmetrical
1272 distribution of receivers (gray triangles in Figure S5) is chosen to eliminate effects due to
1273 station geometry. A grid-search, using a global 1D model (ak135), is performed around
1274 the true hypocenter, with a resolution of 1 km in latitude and longitude and 0.1 s in origin
1275 time. The focal depth is fixed to 10 km, though tests with floating focal depths show only
1276 biases in origin time. Gray arrows in Figure S5 indicate direction and amplitude of
1277 epicenter-mislocations due to the effect of unmodeled source-side 3D velocity structure.
1278 In general, solutions in the 1D model tend to locate north of their 3D location with a
1279 mean mislocation of about 5 km.

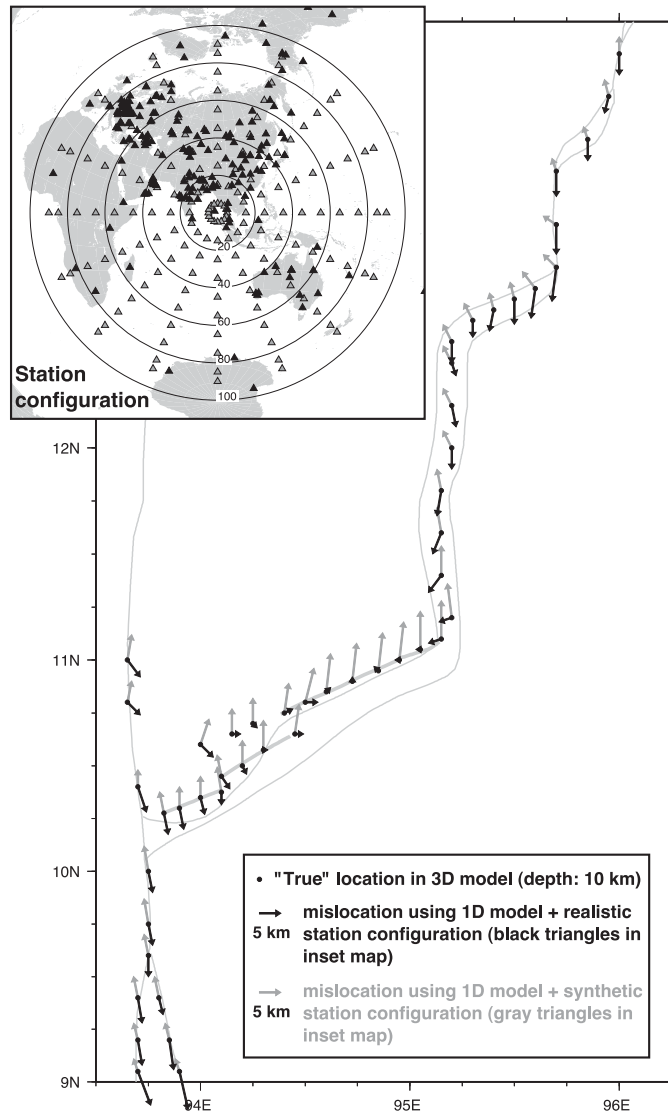
1280

1281 To assess the additional effect of the network geometry, travel times are calculated for
1282 the same set of sources in the 3D model, using a realistic station distribution (black
1283 triangles in Figure S5) taken from an earthquake in the Andaman Spreading Center
1284 ($m_b=5.1$). Only stations reporting *P* phase picks in the ISC bulletin are considered. The
1285 combined effect of 3D structure and network geometry is shown in Figure S5 by black
1286 arrows. Along the central and the eastern segment of the spreading center, the effect of
1287 network geometry compensates the mislocation caused by unmodeled 3D structure, and
1288 the net mislocation is smaller than 1 km. Mean shift in origin time is on the order of -1 s
1289 in both tests. Systematic errors in absolute location caused by the combined effect of

1290 unmodeled 3D velocity structure and potential bias due to heterogeneous station
1291 distribution are less than 1 km in longitude and less than 5 km in latitude for most parts of
1292 the Andaman Sea. EHB epicenters might be located slightly south of their true location.

1293

1294 Effects of the 3D velocity structure on the absolute focal depths were not explicitly
1295 studied in this test. The absolute depths of the initial locations strongly depend on depth
1296 phases. Relative depths, however, are reasonably well constrained because of the
1297 differential core phases with their steep takeoff angles. Insufficient linkage of depth and
1298 core phases can result in poorly constrained focal depth of individual earthquakes.



1299

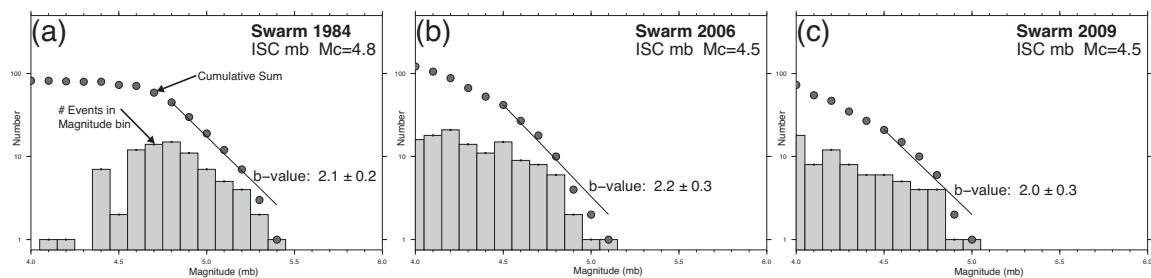
1300 **Figure S5.** Arrows indicate direction and amplitude of absolute mislocation of epicenters (in kilometers) caused by using a global 1D
 1301 velocity model (ak135). Gray arrows correspond to a synthetic station configuration (gray triangles in inset map), reflecting pure
 1302 model effects. Black arrows correspond to a realistic station configuration (black triangles in inset map), reflecting combined effect of
 1303 3D structure and network geometry. Position of synthetic hypocenters is indicated by black dots. Tectonic features (after *Curry*
 1304 [2005]) are indicated by thin gray lines, ridge segments as defined by *Kamesh Raju et al.* [2004] are indicated by bold gray lines.
 1305 Circles in inset map correspond to great-circle distances in degree.

1306

1307 **S.3 b-value analysis**

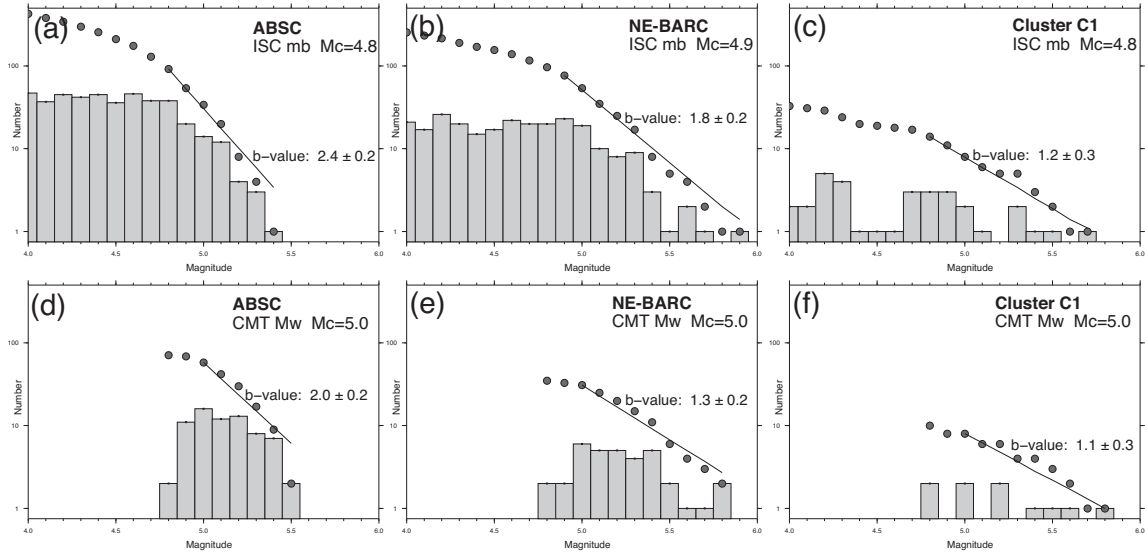
1308 The frequency-magnitude distribution describes the relationship between the frequency
 1309 of occurrence and the magnitude of earthquakes. The b-value describes the relative size

1310 distribution of events and can be indicative of the material's heterogeneity, increase in
 1311 pore pressure, or the stress regime [e.g., Mogi, 1962; Wiemer et al., 1998; Schorlemer et
 1312 al., 2005]. To see if differences in the frequency-magnitude distribution exist, we
 1313 calculated b-values for different parts of the back-arc region by using a maximum-
 1314 likelihood technique [e.g. *Aki, 1965; Bender, 1983; Woessner and Wiemer, 2005*]. The
 1315 magnitude of completeness (M_c) was determined visually by assessing the cumulative
 1316 sum as well as the absolute number of magnitudes in the magnitude bins. Due to the
 1317 narrow range in magnitudes and the relatively small number of events, the derived b-
 1318 values likely have large uncertainties and should only be considered “suggestive”. The
 1319 results are very sensitive to M_c , which is difficult to determine in case of such narrow
 1320 range in magnitude and the small number of events. Figure S6 shows individual b-values
 1321 for the three major swarms in the ABSC derived from mb as reported in the ISC catalog.
 1322 Figure S7 shows b-values for three different sub-regions in the back-arc derived from mb
 1323 in the ISC catalog and M_w in the global CMT catalog. Our results suggest that b-values
 1324 in the ABSC appear to be higher than anywhere else in the back-arc region. As for other
 1325 volcanic regions in the world, the high b-values might be indicative for active volcanic
 1326 processes in the ABSC.



1327
 1328
 1329
 1330

Figure S6. b-values for three major swarms in the ABSC derived from mb as reported in the ISC catalog. Dots indicate cumulative sum of magnitude readings, histograms indicate absolute number of magnitude reading per magnitude bin.



1331

1332 **Figure S7.** b-values for three different sub-regions in the back-arc derived from mb in the ISC catalog (a-c) and Mw in the global
 1333 CMT catalog (d-f). Dots indicate cumulative sum of magnitude readings, histograms indicate absolute number of magnitude reading
 1334 per magnitude bin. b-values in the ABSC appear higher than elsewhere in the back-arc region.

1335

1336 **S.4 CLVD analysis of global CMT solutions**

1337 The non-double-couple part of the moment tensor is described by the compensated-
 1338 linear-vector-dipole (CLVD) component [Knopoff and Randall, 1970; Frohlich, 1990].

1339 Special types of non-double-couple mechanisms are vertical-CLVD earthquakes, which
 1340 have large non-double-couple component and steeply plunging P- or T-axis. Such

1341 vertical-CLVD earthquakes often correlate in space and time with episodes of volcanic
 1342 unrest and are interpreted to be the result of volcanic processes [e.g., Ekström, 1994;

1343 Nettles and Ekström, 1998; Shuler et al., 2013]. One of the physical models proposed for
 1344 such vertical-CLVD mechanisms suggests dip-slip motion on volcano ring faults

1345 [Ekström, 1994].

1346

1347 To see whether or not such vertical-CLVD mechanisms exist in the back-arc region we
1348 analyzed moment tensor solutions in the global CMT catalog following the approach of
1349 *Shuler et al.* [2013]. The non-double-couple component is defined as

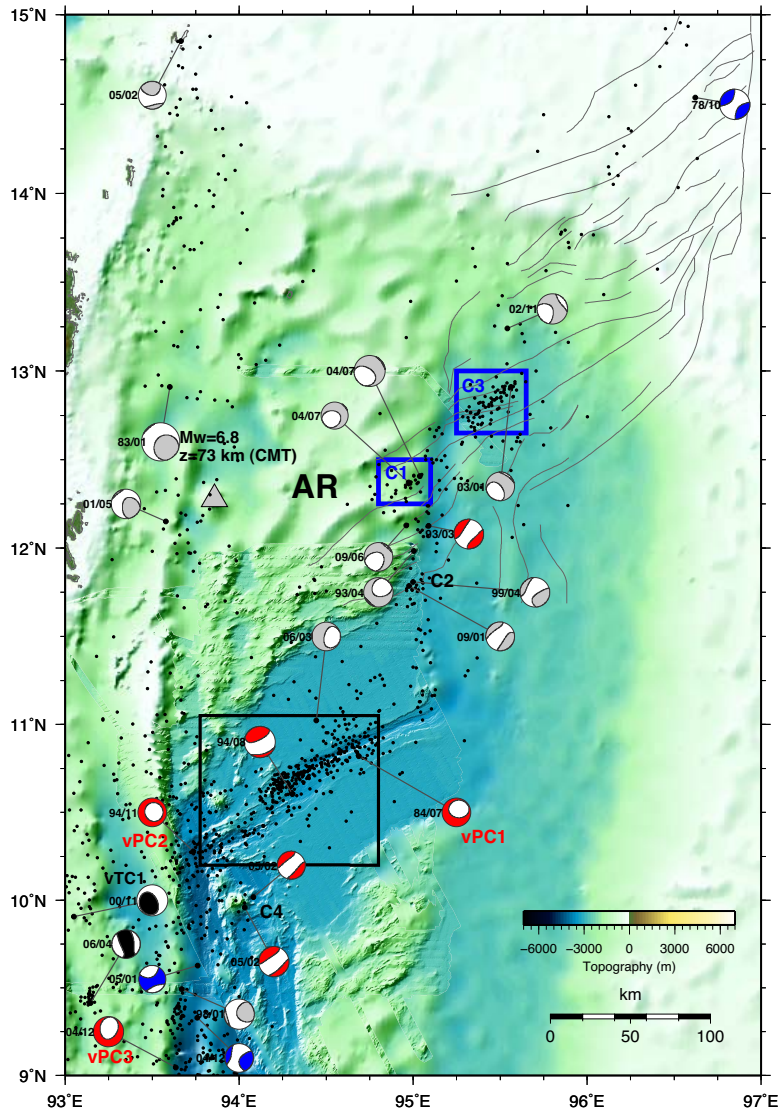
1350

$$1351 \quad \varepsilon = -\lambda_2 / \max(|\lambda_1|, |\lambda_3|),$$

1352

1353 where λ_1 is the largest eigenvalue, λ_3 is the smallest eigenvalue, and λ_2 is the
1354 intermediate eigenvalue of the moment tensor. Pure double-couple earthquakes have $\varepsilon=0$
1355 and pure CLVD mechanisms have $\varepsilon=\pm 0.5$. Following *Shuler et al.* [2013] we calculated ε
1356 for all moment tensors in the global CMT catalog, which are within the back-arc region.
1357 We found 24 solutions with $|\varepsilon| > 0.2$, which are shown in Figure S8. Only 3 of those
1358 events are located within the ABSC region. Using the definition for vertical-P CLVD
1359 events ($\varepsilon < -0.2$, plunge of P-axis $>60^\circ$) of *Shuler et al.* [2013] we found three of such
1360 events in the back-arc region (vPC1-vPC3 in Figure S8). Only one of them (vPC1) is
1361 located within the ABSC and part of the 1984 swarm. In addition, we found one vertical-
1362 T CLVD event ($\varepsilon > +0.2$, plunge of T-axis $>60^\circ$) in the back-arc region (vTC1 in Figure
1363 S8), which is probably related to the plate interface. *Shuler et al.* [2013] pointed out that
1364 adding additional mantle-wave and surface-wave data can significantly reduces the size
1365 of the CLVD component of the CMT solution. Therefore we cannot rule out the
1366 possibility that some of the events shown in Figure S8 are in fact close to double-couple
1367 mechanisms.

1368



1369

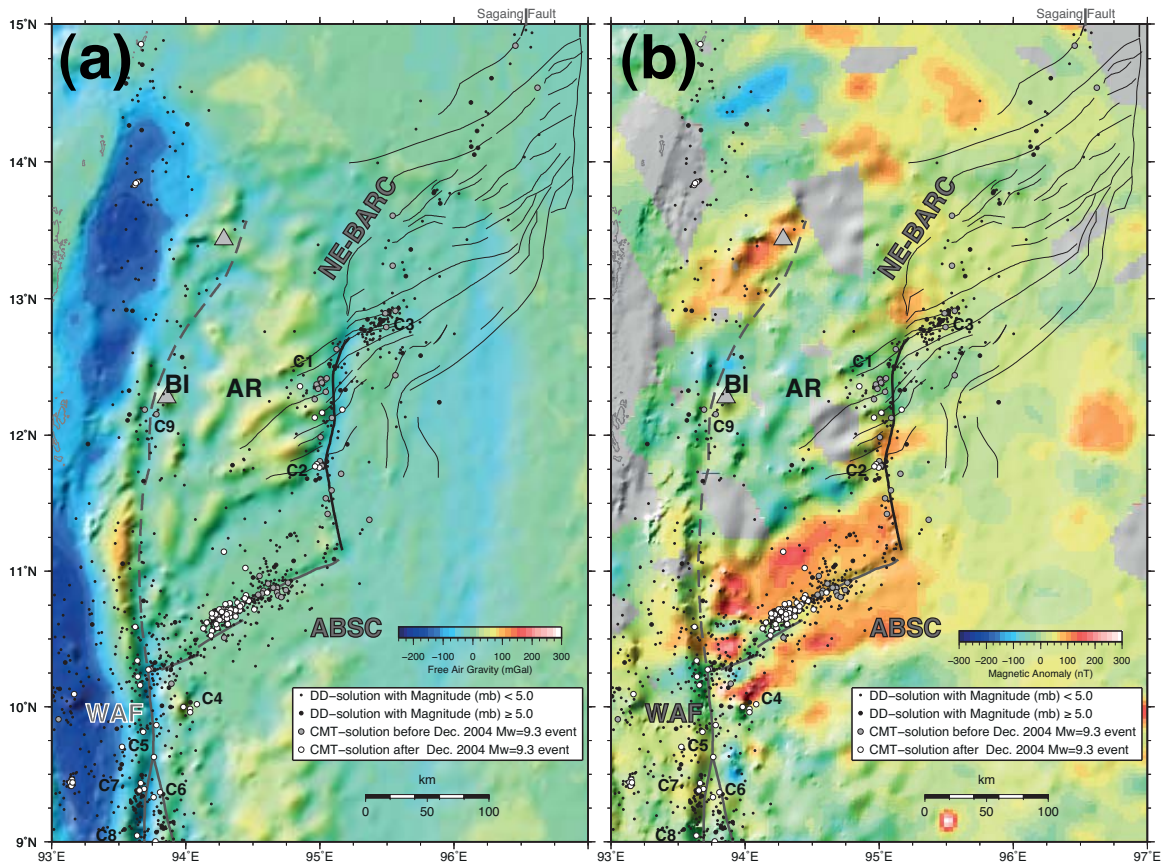
1370 **Figure S8.** CMT solutions with significant non-double-couple components ($|c| > 0.2$) in the back-arc region. Label left of beach-ball
 1371 symbols denotes year/month of event. Mechanisms labeled vPC1-vPC3 fall in the category of vertical-P CLVD earthquakes,
 1372 mechanism labeled vTC1 falls in the category of a vertical-T CLVD earthquake.

1373

1374 **S.5 Regional gravity and magnetic anomalies**

1375 In Figure S9 we overlay regional free-air gravity [*Sandwell and Smith, 2009*] and
 1376 magnetic anomalies [*Maus et al., 2009*] with the relocated seismicity of this study. The
 1377 north-south striking negative anomaly in the gravity data in-between the Andaman
 1378 Islands and the WAF (Figure S9a) was previously interpreted by *Curray [2005]* as

1379 indication for low-density sediments in the accretionary complex. The positive anomaly
 1380 around 93.5°E/11.25°N, on the other hand, was interpreted as uplifted volcanics and/or
 1381 intrusives [Curray, 2005]. The magnetic data in Figure S9b features an area of high
 1382 magnetization over the ABSC, which probably reflects the presence of younger, highly
 1383 magnetic crust in that region.



1384
 1385 **Figure S9.** (a) Satellite-derived free-air gravity anomalies [Sandwell and Smith, 2009], draped over bathymetric relief. Dots indicate
 1386 relocated seismicity in the back-arc region. White and gray dots indicate events with CMT solutions. (b) Magnetic anomaly data
 1387 (EMAG2 V2, Maus et al. [2009]) draped over bathymetric relief.

1388
 1389
 1390
 1391

1392 **S.6 Coulomb stress change modeling**

1393 In order to compare the amplitudes of the post-2004 regional stress change (in the order
1394 of 0.2-0.3 bar) to local stresses resulting from a dike intrusion, we modeled the Coulomb
1395 stress change due to a hypothetical tensile opening at the location of the 2006 earthquake
1396 swarm. We used two different receiver fault geometries based on the CMT solutions
1397 displayed in Figure 10:

1398 - Steeply dipping axial faults (average for axial events):

1399 strike= 73° , dip= 58° , rake= -92°

1400 - Moderately dipping off-axis faults (average for events in fault-scarp region):

1401 strike= 63° , dip= 36° , rake= -96°

1402 The finding of the modeling is that local stress changes due to a hypothetical intrusion
1403 significantly exceed possible coseismic stress perturbations that may have originated
1404 from the Dec. 2004 rupture. The difference in stress change is in the order of one
1405 magnitude and this finding is rather independent from the parameters used in the
1406 modeling as shown by Figure S10. Figure S10a shows the Coulomb stress change at 1 km
1407 depth using the parameters described in section 4.3 of the paper:

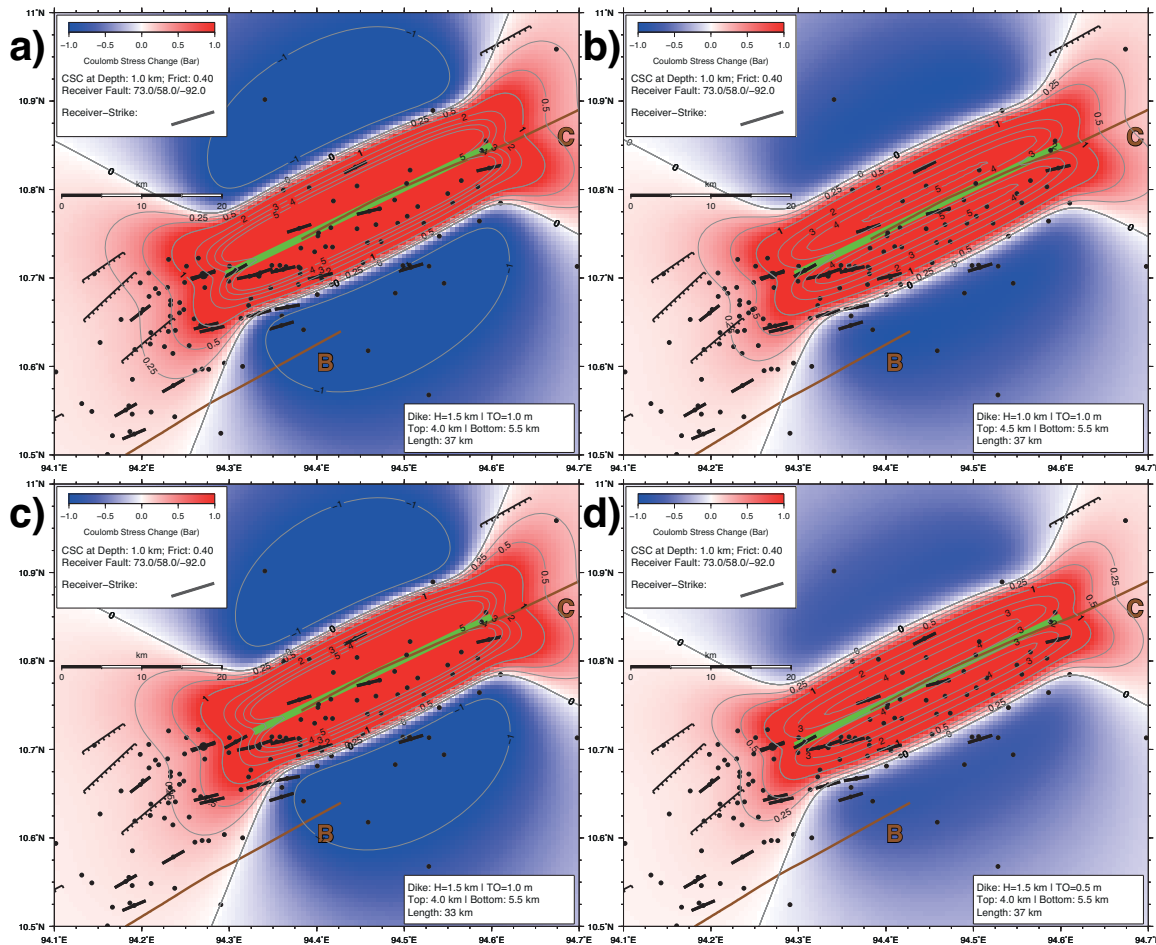
1408 - Tensile opening of 1 m: Typical values found in literature.

1409 - Dike height: 1.5 km (from 5.5 km to 4 km depth): Typical values found in literature.

1410 - Along-strike length of dike 37 km: Based on extent of axial seismicity in the first 4
1411 hours of the 2006 swarm.

1412 Most axial events are included within the 5 bar isoline. Parameters used in Figure S10b
1413 are identical to S10a, except that the dike height was reduced to 1 km (from 5.5 km to 4.5
1414 km depth). Most axial events are located within the 1-2 bar isoline. In Figure S10c the

1415 along-strike length of the dike was reduced to 33 km and in Figure S10d the tensile
 1416 opening was reduced to 0.5 m. In both cases, the majority of the axial events are located
 1417 within the 1-2 bar isoline. In all models, axial events are located within the 1-2 bar isoline
 1418 and stress change amplitudes significantly exceed the 0.2-0.3 bar predicted by coseismic
 1419 stress models for the Dec. 2004 rupture. Perturbations in the modeled dike geometry
 1420 mainly affect the stress change amplitudes in the off-axis regions.



1421
 1422 **Figure S10.** Results of the Coulomb stress modeling for different dike geometries along segment C of the ABSC. The green line
 1423 indicates the along strike extent of the hypothetical dike, black dots indicate epicenters of the 2006 earthquake swarm, black bars
 1424 indicate direction of CMT B-axes. Faults identified from high-resolution bathymetric data are shown by black. (a) Dike geometry
 1425 described in section 4.3 of the paper. (b) Dike height reduced to 1 km. (c) Along-strike extent reduced to 33 km. (d) Tensile opening
 1426 reduced to 0.5 m.
 1427

1428

References (Electronic Supplement)

- 1429 Aki, K. (1965), Maximum likelihood estimate of b in the formula $\log N = a - bM$ and its
1430 confidence limits, *Bull. Earthq. Res. Inst. Tokyo Univ.*, *43*, 237–239.
- 1431 Bender, B. (1983). Maximum likelihood estimation of b -values for magnitude grouped
1432 data, *Bull. Seism. Soc. Am.*, *73*, 831–851.
- 1433 Curray, J. R. (2005), Tectonics and history of the Andaman Sea region, *J. Asian Earth*
1434 *Sci.*, *25*(1), 187-228.
- 1435 Ekström, G. (1994), Anomalous earthquakes on volcano ring-fault structures, *Earth*
1436 *Planet. Sci. Lett.*, *128*, 707–712.
- 1437 Frohlich, C. (1990), Earthquakes with non-double-couple mechanisms, *Science*, *264*,
1438 804–809.
- 1439 Kamesh Raju, K. A., T. Ramprasad, P. S. Rao, B. R. Rao, and J. Varghese (2004), New
1440 insights into the tectonic evolution of the Andaman basin, northeast Indian Ocean, *Earth*
1441 *Planet Sci. Lett.*, *221*(1-4), 145-162.
- 1442 Knopoff, L., and M. J. Randall (1970), The compensated linear-vector dipole: A possible
1443 mechanism for deep earthquakes, *J. Geophys. Res.*, *75*(26), 4957–4963.
- 1444 Maus, S. et al. (2009), EMAG2: A 2-arc min resolution Earth magnetic anomaly grid
1445 compiled from satellite, airborne, and marine magnetic measurements, *Geochem.*
1446 *Geophys. Geosyst.*, *10*(Q08005), doi:10.1029/2009GC002471.

1447 Mogi, K. (1962), Magnitude-frequency relations for elastic shocks accompanying
1448 fractures of various materials and some related problems in earthquakes, *Bull. Earthq.*
1449 *Res. Inst. Tokyo Univ.*, 40, 831-853.

1450 Nettles, M., and G. Ekström (1998), Faulting mechanism of anomalous earthquakes near
1451 Bárðarbunga Volcano, Iceland, *J. Geophys. Res.*, 103(B8), 17,973–17,983.

1452 Sandwell, D., and W. Smith (2009), Global marine gravity from retracked Geosat and
1453 ERS-1 altimetry: ridge segmentation versus spreading rate, *J. geophys. Res.*,
1454 114(B01411), doi:10.1029/2008JB006008.

1455 Schorlemmer, D., S. Wiemer, and M. Wyss (2005), Variations in earthquake-size
1456 distribution across different stress regimes, *Nature*, 437, 539-542.

1457 Shuler, A., M. Nettles, and G. Ekström (2013), Global observation of vertical-CLVD
1458 earthquakes at active volcanoes, *J. Geophys. Res. Solid Earth*, 118,
1459 doi:10.1029/2012JB009721.

1460 Widiyantoro, S., and R. van der Hilst (1997), Mantle structure beneath Indonesia inferred
1461 from high-resolution tomographic imaging, *Geophys. J. Int.*, 130(1), 167-182.
1462

1463 Wiemer, S., S. McNutt, and M. Wyss (1998), Temporal and threedimensional spatial
1464 analyses of the frequency-magnitude distribution near Long Valley Caldera, California,
1465 *Geophys. J. Int.*, 134, 409–421, doi:10.1046/j.1365-246x.1998.00561.x.
1466

1467 Woessner, J. and S. Wiemer (2005), Assessing the quality of earthquake catalogues:
1468 estimating the magnitude of completeness and its uncertainty, *Bull. Seism. Soc. Am.*, 95,
1469 684–698.